DETAILED SHAPE AND EVOLUTIONARY BEHAVIOR OF THE X-RAY LUMINOSITY FUNCTION OF ACTIVE GALACTIC NUCLEI

T. Miyaji[1,2,15], G. Hasinger[3], M. Salvato[4], M. Brusa[4,5,6], N. Cappelluti[6], F. Civano[7,8], S. Puccetti[9], M. Elvis[8],
H. Brunner[4], S. Fotopoulou[10], Y. Ueda[11], R. E. Griffiths[12], A. M. Koekemoer[13], M. Akiyama[14], A. Comastri[6], R. Gilli[6],
G. Lanzuisi[6], A. Merloni[4], AND C. Vignali[5,6]

[1] Instituto de Astronomía sede Ensenada, Universidad Nacional Autónoma de México, Km. 103,
Carret. Tijuana-Ensenada, Ensenada, BC 22860, Mexico; miyaji@astrosen.unam.mx
[2] University of California San Diego, Center for Astrophysics and Space Sciences, 9500 Gilman Drive, La Jolla, CA 92093-0424, USA
[3] Institute for Astronomy, 2680 Woodlawn Drive, University of Hawaii, Honolulu, HI 96822, USA; hasinger@ifa.hawaii.edu
[4] Max-Planck-Institut für extraterrestrische Physik, Giessenbachstrasse 1, D-85748 Garching bei München, Germany
[5] DIFA—Dipartimento di Fisica e Astronomia, Universita' di Bologna, viale Berto Pichat 6/2, I-40127 Bologna, Italy
[6] INAF-Osservatorio Astronomico di Bologna, via Ranzani 1, I-40127 Bologna, Italy
[7] Yale Center for Astronomy and Astrophysics, 260 Whitney Avenue, New Haven, CT 06520, USA
[8] Smithsonian Astrophysical Observatory, 60 Garden Street, Cambridge, MA 02138, USA
[9] ASI Science Data Center, via Galileo Galilei, I-00044, Frascati, Italy
[10] University of Geneva, chemin d Ecogia 16, 1290 Versoix, Switzerland
[11] Department of Astronomy, Faculty of Science, Kyoto University, Kitashirakawa-Oiwake-cho,Sakyo-ku, Kyoto 606-8502, Japan
[12] Physics & Astronomy, STB-216, U. Hawaii at Hilo, Hilo, HI 96720, USA
[13] Space Telescope Science Institute, 3700 San Martin Drive, Baltimore, MD 21218, USA
[14] Astronomical Institute, Tohoku University, 6-3 Aramaki, Aoba-ku, Sendai 980-8578, Japan

ABSTRACT

We construct the rest-frame 2–10 keV intrinsic X-ray luminosity function (XLF) of active galactic nuclei (AGNs) from a combination of X-ray surveys from the all-sky *Swift* BAT survey to the *Chandra* Deep Field South. We use ~3200 AGNs in our analysis, which covers six orders of magnitude in flux. The inclusion of *XMM* and *Chandra* COSMOS data has allowed us to investigate the detailed behavior of the XLF and evolution. In deriving our XLF, we take into account realistic AGN spectrum templates, absorption corrections, and probability density distributions in photometric redshift. We present an analytical expression for the overall behavior of the XLF in terms of the luminosity-dependent density evolution, smoothed two-power-law expressions in 11 redshift shells, three-segment power-law expression of the number density evolution in four luminosity classes, and binned XLF. We observe a sudden flattening of the low luminosity end slope of the XLF slope at $z \gtrsim 0.6$. Detailed structures of the AGN downsizing have also been revealed, where the number density curves have two clear breaks at all luminosity classes above $\log L_X > 43$. The two-break structure is suggestive of two-phase AGN evolution, consisting of major merger triggering and secular processes.

Key words: galaxies: active – galaxies: luminosity function, mass function – quasars: general – X-rays: galaxies

1. INTRODUCTION

The active galactic nucleus (AGN)/QSO luminosity function and its evolution with cosmic time are key observational quantities for understanding the origin of supermassive black holes (SMBHs) and accretion onto them. The luminosity function is one of the most important observational products, along with the demography of SMBHs, which are made by scaling relations with host galaxy properties (e.g., Magorrian et al. 1998; Häring and Rix 2004; Gültekin et al. 2009; see Kormendy & Ho 2013 for recent review), as well as emerging AGN-clustering measurements, which locate typical masses of dark matter halos (DMHs) in which the AGNs reside (e.g., Mullis et al. 2004; Yang et al. 2006; Coil et al. 2009; Gilli et al. 2009; Cappelluti et al. 2010; Krumpe et al. 2010, 2012) or the halo occupation distribution (e.g., Miyaji et al. 2011; Allevato et al. 2012; Chatterjee et al. 2013; Richardson et al. 2013).

X-ray surveys are practically the most efficient means of finding AGNs over a wide range of luminosity and redshift. X-ray emission from almost all extragalactic point X-ray sources with luminosities of $L_X \gtrsim 10^{42} \mathrm{erg\ s^{-1}}$ are considered to originate from SMBH accretion because X-ray emission from

the star formation origin (through supernova remnants and X-ray binaries) of galaxies with the highest star formation rates typically has a luminosity lower than this (Persic et al. 2004; Ranalli et al. 2005; Ptak et al. 2007). Enormous efforts have been made by several groups to follow up the survey X-ray sources with major optical telescopes around the globe, so that we have fairly complete samples of X-ray-selected AGNs (Brandt & Hasinger 2005, for review). One of the most important products of such X-ray AGN surveys is the X-ray luminosity function (XLF) and its evolution with cosmic time. Since X-ray emission marks the accretion activity onto the SMBHs, the XLF and its evolution gives a bird's eye view of the moments of SMBH growth process.

The launch of *ROSAT* and the enormous optical followup efforts of the X-ray sources detected by this satellite enabled us, for the first time, to probe the X-ray-emitting AGN populations to highly cosmological distances. From the mid-1990s to mid-2000s, the evolution of the XLF in the soft band (0.5–2 keV) was investigated by numerous authors (e.g., Boyle et al. 1993; Jones et al. 1997; Page et al. 1997; Miyaji et al. 2000a, 2001; Hasinger et al. 2005). While the soft-band surveys found predominantly unobscured (type 1) AGNs except at very high redshifts, imaging surveys at $2 < E\ [\mathrm{keV}] \lesssim 10$ with *ASCA*,

XMM-Newton, and *Chandra* enabled us to expand the investigation to include obscured (type 2) AGNs, predominantly within the Compton-thin (CTN) limit $(\log N_{\rm H} \left[{\rm cm}^{-2}\right] \lesssim 24)$, providing a view of the SMBH accretion process with much better sampling. Analysis of the $2 < E\,[{\rm keV}] \lesssim 10$ XLF has been made by various groups using different samples with different approaches and different levels of sophistication (e.g., Cowie et al. 2003; Ueda et al. 2003, 2014; La Franca et al. 2005; Silverman et al. 2008; Ebrero et al. 2009; Yencho et al. 2009; Aird et al. 2010). Many groups took a simple approach and constructed the 2–10 keV XLF, assuming a simple power-law spectrum without absorption corrections. From the combination of AGNs from *HEAO-1*, *ASCA*, and early *Chandra* survey samples, Ueda et al. (2003) constructed an absorption-corrected 2–10 keV XLF with a full $N_{\rm H}$ function, as well as a new AGN population synthesis model of the X-ray background. This work was recently revised by Ueda et al. (2014, hereafter, U14), which included both soft and hard samples from diverse sources derived from *ROSAT*, *MAXI*, *ASCA*, *XMM-Newton*, and *Chandra* surveys. U14 included sophisticated spectral model templates, a revised population synthesis model, discussions on possible contributions from Compton-thick (CTK) AGNs, as well as the growth of SMBHs. A few works have included absorption into analysis (La Franca et al. 2005; Ebrero et al. 2009). Aird et al. (2010) took a simpler approach in spectral assumptions, but used sophisticated statistical techniques and took into account the probability density distribution function (PDF) of photometric redshifts and incompleteness corrections, with Bayesian and Markov Chain Monte Carlo methods in their model parameter search. In an attempt to make the XLF construction as free from absorption corrections as possible, Fotopoulou et al. (2015) restricted their analysis to the 5–10 keV band and used the full Bayesian approach in obtaining parameter constraints.

Most authors fitted their XLFs to simple analytical formulae. As a common feature of most such models, the XLF at a given redshift has a (smoothed) two-power-law form with a shallower slope at the low-luminosity end and a steeper slope at the high-luminosity end. This is quite unlike the Schechter function, which is customarily used to describe the optical luminosity function of galaxies and has an exponential decline at higher luminosities. As for the XLF evolution, early evolution models with the pure luminosity evolution scheme (PLE; e.g., Boyle et al. 1993; Page et al. 1997) have been superseded by more complex expressions. Many authors have used the Luminosity-Dependent Density Evolution (LDDE; e.g., Schmidt & Green 1983; Miyaji et al. 2000a; Ueda et al. 2003; Hasinger et al. 2005) model of one form or another. Yencho et al. (2009) and Aird et al. (2010) considered the models where a smoothed two-power-law XLF evolves both in the luminosity and density directions, keeping the XLF shape the same. These are called the (Independent) Luminosity And Density Evolution (called the ILDE or LADE) models. Because the change of at least the low-luminosity slope with redshift is observed to be present, generally, the LDDE model is preferred, as critically compared by Fotopoulou et al. (2015).

When AGN number densities are viewed as a function of redshift in different luminosity classes, the AGNs evolve in an "antihierarchical" manner or show "AGN downsizing" (e.g., Cowie et al. 2003; Ueda et al. 2003; Hasinger et al. 2005); that is, the peak of the AGN number density appears at lower redshifts for low-luminosity AGNs than those with high luminosities. This was in contrast to an early theoretical prediction based on AGN triggering by hierarchical merging (Wyithe & Loeb 2003), in which it was predicted that lower-luminosity AGNs peak at higher redshifts (or emerge earlier in the cosmic history). In recent years, there has been growing support for the hypothesis that the AGN population might be composed of two populations that have been triggered by different mechanisms. One is a major merger-driven triggering, which mainly accounts for high-luminosity QSOs and is dominant in high redshifts. The other is a secular process, which might include fly-by encounters, minor mergers, and/or disk instabilities and is dominant in intermediate-low luminosity (e.g., Draper & Ballantyne 2012; Georgakakis et al. 2014). A number of theoretical works, involving cosmological N-body and/or N-body+hydrodynamical simulations and semianalytical treatments in identifying AGNs, have reproduced and/or explained this AGN downsizing effect (e.g., Di Matteo et al. 2003; Hopkins et al. 2005; Marulli et al. 2008; Croton 2009; Degraf et al. 2010; Fanidakis et al. 2012).

Some models also include "radio mode" (a.k.a., "hot halo" mode). Fanidakis et al. (2012) put emphasis on dividing the AGN activity into "starburst mode," which includes SMBH accretion following both merger-driven and disk-instability-driven starbursts, and the "hot halo" mode. By also including the empirical obscuration effect, they reproduced the AGN downsizing effect. With this general scheme, Fanidakis et al. (2013) explained the tendency that intermediate X-ray luminosity AGNs are associated with more massive dark matter halos (DMHs) than luminous QSOs (Miyaji et al. 2007; Krumpe et al. 2010; Allevato et al. 2011; Krumpe et al. 2012). In order to critically compare these lines of theories and observation, refinements in calculations of the XLF and investigating its detailed evolutionary behavior continues to be an important observational task.

In this work, we use AGNs selected at $E > 2\,{\rm keV}$ from a collection of surveys. Our aim is to construct and investigate the detailed behavior of the XLF. In this particular work, we make our best effort to construct the luminosity function of unabsorbed and absorbed AGNs within the CTN limit, i.e., absorbing column densities of $\log N_{\rm H}\left[{\rm cm}^{-2}\right] \lesssim 24$. Above this column density, Compton scattering causes photons to travel along longer paths within the absorbing medium and are subject to much higher chance of photoelectric absorption. In such CTK AGNs, X-ray emission at $E \lesssim 10$ keV, which is observable with *ASCA*, *XMM-Newton*, and *Chandra*, is highly suppressed unless they are at very high redshifts. Thus AGNs detected in the $E \lesssim 10$ keV surveys are considered to be dominated by CTN AGNs, with the exception of a small number of X-ray sources, for which X-ray emission is dominated by scattered and reflected components (Brunner et al. 2008; Brightman & Ueda 2012; Brightman et al. 2014). In the local universe, higher-energy X-ray surveys $(20 \lesssim E \lesssim 200\,{\rm keV})$, such as those available from *Swift* BAT (e.g., Tueller et al. 2010; Ajello et al. 2012) and *INTEGRAL* (e.g., Beckmann et al. 2009; Treister et al. 2009), can modestly detect CTK AGNs $24 \lesssim \log N_{\rm H}\left[{\rm cm}^{-2}\right] \lesssim 25$ and quantify their space density and emissivities. *NuSTAR* (e.g., Alexander et al. 2013) is extending this to higher redshifts ($z \sim 0.5$–1).

We present here a new estimate of the XLF evaluated at the traditional 2–10 keV rest frame. Complementary to a recent work by Ueda et al. (2014), whose emphasis is on the X-ray

population synthesis of the X-ray background, as well as discussions on the role of the CTK AGNs, our emphasis is on the detailed behavior of the shape and evolution of the XLF, as well as discussions of possible systematic errors. In particular, in order to assess the uncertainties due to photometric redshifts, we include the PDFs of photometric redshifts (photo-z's) into analysis and compare with the results obtained by using single best-fit photo-z's. We focus on the XLF of unabsorbed and CTN AGNs because of the wide availability of $E \lesssim 10$ [keV] AGNs. Additionally, X-ray luminosity L_X, which is the independent variable of the XLF presented in this paper, is primarily defined as the *intrinsic* 2–10 keV luminosity, i.e., before absorption and not including the reflection component.

In this work, the sample is greatly expanded by the addition of the data sets from *XMM*-COSMOS (Hasinger et al. 2007) and C-COSMOS (Elvis et al. 2009), which are parts of the COSMic evolution Survey (COSMOS; Scoville et al. 2007). In Section 2, we explain our COSMOS sample, including the construction of our combination of the *XMM*-COSMOS and C-COSMOS data sets. The details of the selection criteria for other samples from the literature are explained in Section 3. At the end of this section, we explain our incompleteness correction and derive the $N(>S)$ function for extragalactic X-ray sources in each sample.

In Section 4, we explain the computation of our estimated XLFs. Model parameter estimations using a maximum-like-lihood (ML) fitting method, which also include absorption and the probability density distributions (pz-PDFs) of photometric redshifts, are explained. This section also covers the N_{obs}/N_{mdl} estimation of the binned XLF in the presence of the absorption and pz-PDFs.

Section 5 presents our global expression of the LDDE. In Section 6, we take a closer look at detailed behavior of the XLF in redshift-divided shells and the number density/emissivity evolution in luminosity-divided classes. We also present binned XLFs. The results are discussed in Section 7 and a concluding summary is given in Section 8.

Throughout this work we use a Hubble constant, $H_0 = 70h_{70}$ km s^{-1} Mpc^{-1} $\Omega_m = 0.3$, and $\Omega_\Lambda = 0.7$. The h_{70} dependence is explicitly stated. If units are omitted, X-ray luminosities (L with any subscripts/superscripts) are measured in units of h_{70}^{-2} erg s^{-1}, and column densities, N_H, in cm^{-2}. The symbol log signifies a base-10 logarithm, and ln signifies a natural logarithm.

2. COSMOS SAMPLE

2.1. XMM-COSMOS Sample

As a part of the COSMOS collaboration, the *XMM*-COSMOS program (PI, G. Hasinger; Hasinger et al. 2007) included observations of the entire 2.14 deg^2 COSMOS field with the EPIC camera on board the *XMM-Newton* observatory over three observing cycles, AO-3, 4, and 6. X-ray point source catalogs have been produced using a sophisticated source detection and characterization procedure (Cappelluti et al. 2007, 2009). The procedure was developed as a part of the *XMM*-SAS package.[16] In the combined data set, which is composed of 55 *XMM-Newton* observations with a total exposure of ~1.5 Ms, 1887 unique X-ray sources have been detected. Optical counterparts and their multiwavelength

properties were published for the X-ray source detected in the first 12 *XMM-Newton* observations by Brusa et al. (2007) and for all 53 successful observations made before 2007 by Brusa et al. (2010).

In this work, we use X-ray sources detected in the hard (EPIC energy channel between 2 and 8 keV) band in the 53 *XMM*-COSMOS observations with a maximum likelihood of ML > 10, which corresponds to the false detection probability of $e^{-10} \approx 4.5 \times 10^{-5}$. Brusa et al. (2010) published a multiwavelength catalog for the 53-field *XMM*-COSMOS sources with a primary 2–10 keV flux cut of $S_X \geqslant 3 \times 10^{-15}$ erg s^{-1} cm^{-2}, which is our *XMM*-COSMOS base catalog. After this flux cut, we are left with 923 hard-band-selected *XMM*-COSMOS sources. We use the EPIC 2–8 keV count rate to the 2–10 keV flux energy conversion factor (hereafter referred to as ECF) obtained by assuming a power-law spectrum with photon index $\Gamma = 1.7$ absorbed by a Galactic absorbing column density of $N_H = 2.5 \times 10^{20}$ cm^{-2} (Cappelluti et al. 2009).

2.2. Chandra-COSMOS Sample

With its unprecedented spatial resolution, the *Chandra* X-ray observatory (CXO) provides superb point source sensitivity in deep surveys. The *Chandra* COSMOS program (C-COSMOS, PI, M. Elvis; Elvis et al. 2009) is a large *Chandra* program with a total exposure of ~1.8 Ms, with 49 observations with the ACIS-I instrument. The observed fields are arranged in 7 × 7 overlapping tiles, covering a central 0.9 deg^2 of the COSMOS field. Inclusion of the information obtained by the recent *Chandra* Legacy COSMOS survey (2.5 Ms, PI, F. Civano) will be a topic of a future work. A total of 1781 unique X-ray sources have been detected, with a likelihood threshold of ML > 10.8 in any of the full (0.5–7 keV), soft (0.5–2 keV), or hard (2–7 keV) bands, out of which 1017 are hard-band-detected (Elvis et al. 2009; Puccetti et al. 2009).

In Elvis et al. (2009), the 2–10 keV flux is given for an ECF calculated assuming a $\Gamma = 1.4$ power law. To treat the sample in the same way as *XMM*-COSMOS, we have converted the 2–10 keV flux using the ECF assuming $\Gamma = 1.7$ for our further analysis. Unlike the case of *XMM*-COSMOS, Civano et al. (2012) did not impose any further flux limit in their multiwavelength identification catalog. However, we have imposed a 2–10 keV flux ($\Gamma = 1.7$) limit of $S_X > 1.6 \times 10^{-15}$ erg s^{-1} cm^{-2}, below which the log N − log S curve spuriously rises due to the Eddington bias. This removes the 24 faintest hard-band-detected sources. Note that the log N − log S curve in Figure 9 of Elvis et al. (2009) effectively plots down to this flux level. This leaves 993 C-COSMOS hard-band sources.

2.3. Combined XMM-Chandra COSMOS Sample

2.3.1. Sensitivity Map Combination

In order to take advantage of both the *XMM* and C-COSMOS surveys, we have made a combined sample, which we call the XC-COSMOS sample, by selecting X-ray sources from the more sensitive survey out of the two at any given source position. For this purpose, we have compared the hard X-ray sensitivity map for the 53-field *XMM*-COSMOS survey (Cappelluti et al. 2009) with that for C-COSMOS (Puccetti et al. 2009). The *XMM*-COSMOS sensitivity map has been truncated at the lowest limiting flux of the optical catalog

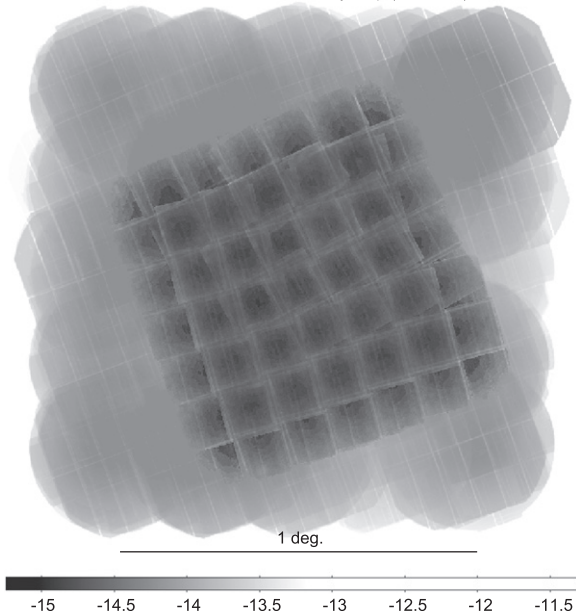---

[16] http://xmm.esac.esa.int/sas/

Figure 1. *XMM*-COSMOS/C-COSMOS combined sensitivity map. The scale indicated by a solid line corresponds to 1° on the sky. The numbers at the tick marks in the gray scale bar at the bottom of the figure indicate the base-10 logarithm of the limiting 2–10 keV flux in units of erg s^{-1} cm^{-2} assuming a $\Gamma = 1.7$ power law.

described above. In order to compare both maps on the same grounds, we scaled the C-COSMOS sensitivity map using the ECF for the photon index of $\Gamma = 1.7$. We further smoothed the C-COSMOS sensitivity map with a Gaussian filter with $\sigma = 16''$ and combined this with the *XMM*-COSMOS sensitivity map by choosing the smaller limiting flux at each point. We have also generated a mask file that indicates whether the *XMM*-COSMOS or C-COSMOS source should be used at each position. In effect, the C-COSMOS sources should be used in most of the region covered by C-COSMOS, except for small areas near the corners and edges. The combined sensitivity map is shown in Figure 1. In the combined sample, there are 1400 extragalactic point sources (mostly AGNs), 18 stars, and 29 unidentified sources. Overall, the fraction of sources identified with AGNs/galaxies with spectroscopic or photometric redshifts and stars is 98%. Note that the XC-COSMOS AGNs comprises as many as ∼43% of all AGNs in our global AGN sample defined below.

One of the greatest advantages of the COSMOS survey is the availability of multiepoch, homogenized, deep 31-band photometry, covering from the UV to the midinfrared wavelengths, including 12 intermediate bands from Subaru (Taniguchi et al. 2007). These data, along with the correction for variability and the use of hybrid AGN templates, have allowed the COSMOS survey to reach a mean photometric redshift accuracy of $\sigma_{\Delta z/(1+z_{\rm spec})} \approx 0.015$ with a low fraction of outliers (∼5%) for both the *XMM* and *Chandra* COSMOS samples (Salvato et al. 2009, 2011). In this work, the newest photometric redshifts by Salvato et al. (2011) have been used when there is no available spectroscopic redshift. The associated probability density distributions of photometric redshifts are also used. In addition to the spectroscopic redshifts included in Brusa et al. (2010), newly available proprietary spectroscopic redshifts from

spectroscopic survey programs within the COSMOS consortium have been included.

3. GLOBAL AGN SAMPLE

3.1. *Swift* BAT Survey Sample

Based on the *Swift* BAT slew scan data accumulated over 60 months, Ajello et al. (2012) produced a catalog of AGNs detected in the 15–55 keV band, providing the current most complete census of nearby bright AGNs over the entire sky. These include unabsorbed and absorbed AGNs up to moderate CTK AGNs. For CTN AGNs, photoelectric absorption has very little effect on the 15–55 keV flux, and thus there is no need for complicated absorption corrections. However, since we are evaluating intrinsic XLF at 2–10 keV, we need a spectral template for unabsorbed AGNs to convert from 15–55 keV to 2–10 keV. In our simplest treatment, we assume a power-law spectrum with a photon index of $\Gamma = 1.7$, which is approximately (within ∼4%) equal to the corresponding ratio for the unabsorbed AGN template spectrum (see Section 4.3). Under this assumption, we can convert the 15–55 keV flux to the 2–10 keV flux by multiplying by a factor of 0.705. In the limiting-flux–survey-area curve from Figure 1 of Ajello et al. (2012), the flux is converted to the 2–10 keV value in this way. In our full treatment in Section 4.3, we use a luminosity-dependent effective photon index for the conversion.

3.2. *ASCA* LSS/MSS

The Advanced Satellite for Cosmology and Astrophysics (*ASCA*) was the first X-ray observatory with focusing optics capable of making spectroscopic imaging in the 2–10 keV band. The combination of *ASCA* Large Sky Survey (ALSS) and the *ASCA* Medium Sensitivity survey (AMSS) fills the gap between all-sky surveys and deeper surveys with *XMM-Newton* and *Chandra*, occupying a unique regime in the z–$L_{\rm X}$ space at $E > 2$ keV.

The ALSS covers a continuous area of 5.5 deg^2 near the North Galactic Pole with a flux limit of $S_{\rm X} \sim 1 \times 10^{-13} \left[{\rm erg~s}^{-1}~{\rm cm}^{-2} \right]$ (2–10 keV) (Ueda et al. 1998, 1999). Thirty AGNs detected with the SIS instrument are completely identified by Akiyama et al. (2000). The AMSS is based on a serendipitous X-ray survey with the GIS instrument (Ueda et al. 2001, 2005) and has a survey area of ∼85 deg^2. The flux limit ranges from 5×10^{-12} to 3×10^{-13} erg s^{-1} cm^{-2}. The identification catalogs in the northern part of the AMSS (Akiyama et al. 2003, AMSSn) and the southern part (AMSSs; M. Akiyama et al. 2015, in preparation) contain 74 and 20 spectroscopically identified nonblazer AGNs, respectively. Three X-ray sources are left unidentified, and the identification completeness is 97% for the combined ALSS and AMSS sample.

The 2–10 keV fluxes of these sources have been obtained from the *ASCA* GIS count rate assuming a $\Gamma = 1.7$ power law using the GIS response matrix.

3.3. *XMM-Newton* Hard Bright Serendipitous Sample

The Hard Bright Serendipitous Sample (HBSS; Della Ceca et al. 2004) is a subsample detected in the 4.5–7.5 keV band from the larger survey of the *XMM-Newton* Bright Survey. Della Ceca et al. (2008) defined a complete flux-limited sample of 67 sources with MOS2 count rates larger than 0.002 $\left[{\rm cts~s}^{-1} \right]$

(4.5–7.5 keV) over 25 deg^2 of the sky. The MOS2 count rates in the HBSS were converted to observed fluxes in the 2–10 keV band, assuming a photon power-law index of 1.7 (using an ECF of 1.044×10^{-11} erg cm^{-2} cts^{-1}). The corresponding flux limit is 2.1×10^{-13} erg s^{-1} cm^{-2}. These sources are completely identified spectroscopically except for two, making the identification completeness ~97%. The 65 identified sources consist of 62 extragalactic point sources (mostly AGNs), two stars, and one cluster of galaxies.

3.4. XMM-Newton Medium-sensitivity Survey

The *XMM-Newton* Medium-sensitivity Survey (XMS; Barcons et al. 2007) is a serendipitous X-ray survey and optical identification program of sources with intermediate X-ray fluxes discovered in 25 *XMM-Newton* high-Galactic-latitude fields covering a sky area of ~3 deg^2. For this analysis the XMS-H sample, selected in the 2–10 keV band, is used. Barcons et al. (2007) assumed a spectral index of $\Gamma = 1.7$ for the count rate-to-flux conversion for the hard band, and therefore we use the 2–10 keV flux as shown in their data set. In our analysis, we use the the subsample of XMS-H defined by Hasinger (2008).

The original Barcons et al. (2007) sample contains 159 sources with 2–10 keV fluxes $>3.3 \times 10^{-14}$ [erg cm^{-2} s^{-1}], with a spectroscopic identification fraction of 83% (27 unidentified sources). However, the actual spectroscopic completeness limit varies from field to field. Therefore, Hasinger (2008) selected a subsample that is comprised of further flux cuts on a field-by-field basis. This way a cleaner XMS sample could be defined, including 128 extragalactic point X-ray sources and almost half the number of unidentified sources, i.e., achieving an identification fraction of 91%. The survey solid angle has been corrected accordingly. See Section 2.4 of Hasinger (2008) for further details.

3.5. Hellas2XMM

HELLAS2XMM (Baldi et al. 2002) is a serendipitous survey based on suitable *XMM-Newton* pointings (complementary to the XMS). The assumed spectral index for the ECF for the 2–10 keV flux in Baldi et al. (2002) was $\Gamma = 1.7$, and therefore we use their flux as provided.

As in the case of the XMS, we use the subsample compiled by Hasinger (2008). Fiore et al. (2003) presented optical identifications and spectroscopic redshifts for 122 sources selected in the 2–10 keV band in five *XMM-Newton* fields, covering a survey area of 0.9 deg^2. Later Maiolino et al. (2006) presented additional redshifts from Very Large Telescope near-infrared spectroscopy of optically extremely faint objects for two additional sources. Both Fiore et al. (2003) and, later, Mignoli et al. (2004) tried to estimate redshifts for the remaining, optically faint, unidentified sources. Cocchia et al. (2007) published photometry and spectroscopic redshifts in five additional HELLAS2XMM fields, providing 59 new redshift identifications for the sample of 110 new sources with an additional solid angle of 0.48 deg^2. As explained in Hasinger (2008), further flux cuts were made on the field-by-field basis. In addition, different flux cuts were applied to the inner and outer regions of each field. The redshift completeness in this subsample of HELLAS2XMM is thus 84%. In this paper, we further raise the flux limit from 1.0×10^{-14} (adopted

by Hasinger 2008) to 1.63×10^{-14} erg s^{-1} cm^{-2} to make the identification 90% complete, leaving 115 AGNs.

3.6. Lockman Hole (XMM)

Because of the extremely low Galactic column density ($N_H = 5.7 \times 10^{19}$ cm^{-2}), Lockman Hole has been selected as a target of X-ray deep survey observations, including a *XMM-Newton* survey (Hasinger et al. 2001; Brunner et al. 2008). The base X-ray source catalog for this work is from Brunner et al. (2008) from 18 individual pointings, 12 of which are centered near the same pointing direction; the remaining pointings are spread out over about ~30′ in right ascension. Brunner et al. (2008) concentrated on the deep central circular area with a radius of 15′ (= 0.20 deg^2). Their catalog contains 409 X-ray sources, out of which 266 are detected in the hard (2–4.5 keV) band at the ML value of 6.0 or above. Based on simulations, they showed that the sources above this ML threshold, in combination with the flux-sensitivity curve in their Figure 5, reproduce the log N − log S accurately.

Their listed 2–10 flux is converted from the EPIC 2–4.5 keV count rate assuming a $\Gamma = 2.0$ power-law spectrum. For our purposes, we have converted their $\Gamma = 2.0$ based 2–10 keV flux to the $\Gamma = 1.7$ based flux using a combined response matrix of the *XMM-Newton* EPIC PN and two MOS detectors. This corresponds to multiplication of the $\Gamma = 2.0$ based flux by 1.16. The limiting-flux–area curve in Figure 5 of Brunner et al. (2008) has also been converted to the $\Gamma = 1.7$ based flux.

Of the 266 hard X-ray-selected sources, 60% have published or unpublished spectroscopic redshifts (including five stars). Including photometric redshifts by Fotopoulou et al. (2012), 98% are identified with either spectroscopic or photometric redshifts. Only four are left unidentified. This results in 257 hard-band-selected extragalactic X-ray point sources. Probability density distributions of the photometric redshifts are also available, which we use in Section 4.2.

3.7. CLASXS and CLANS

The catalogs from two intermediate-depth *Chandra* surveys near the Lockman Hole, the *Chandra* Large Area Synoptic X-ray Survey (CLASXS; Yang et al. 2004), and the *Chandra* Lockman Area North Survey (CLANS; Trouille et al. 2008) are also included in our analysis. The X-ray source identifications and limiting-flux–survey-area curves of both surveys (as well as those of the CDF-N; see below) are conveniently included in Trouille et al. (2008) as a part of their "Opt-X" project. Additional spectroscopic redshifts of CLANS sources can also be found in Trouille et al. (2009). Their tables contain 2–8 keV fluxes based on the 2–8 *Chandra* ACIS-I count rates with the ECFs calculated with variable Γ and ACIS-I response matrices based on old calibrations. Therefore we have converted from their 2–8 keV count rate to the 2–10 keV flux assuming $\Gamma = 1.7$ and with ancillary response files (ARFs) we have recreated for the ACIS-I aim point using the *Chandra* CALDB 4.5.7 (the latest calibration as of our analysis). For each of the CLASXS and CLANS surveys, the applied response is the exposure-weighted average of the responses at the aim points of the observations belonging to the survey. The flux in their limiting-flux–survey-area curves (Figure 5 in Trouille et al. 2008) has been adjusted accordingly. The curves for the probability of detection of 30% are used because they reproduce the log N − log S relation in the simulations by

Yang et al. (2004). Because their curves only apply to the sources with off-axis angles of <8′, we use sources that meet this criterion. Additionally, we only include X-ray sources that are detected at a signal-to-noise ratio of >3 in the hard band in order to be compatible with their flux–survey-area curve. Moreover, in order to be compatible with their flux-limit–area curve, they also imposed off-axis-dependent flux limits to exclude some sources for their $\log N - \log S$ calculations. These imposed limits cannot be reproduced with the published information. However, this effect does not significantly affect our analysis as described below.

In order to minimize the effects of the "completeness correction" (Section 3.12), we impose at least 90% identification completeness for each survey. In order to achieve this, we have excluded the sources with 2–10 keV flux ($\Gamma = 1.7$ based) of $S_X < 6.5 \times 10^{-15}$ and $S < 6.5 \times 10^{-15}$ erg s^{-1} cm^{-2}, leaving 250 and 119 AGNs for CLASXS and CLANS, respectively. At these flux limits, the survey area is already $\sim 95\%$ of the total geometric area, with off-axis angle <8′. Thus the effects of off-axis-dependent flux limits are minimal.

3.8. Chandra Deep Field North (CDF-N)

Our base X-ray source catalog for the 2 Ms CDF-N is from Alexander et al. (2003). As in the cases of CLASXS and CLANS, we have used the hard-band-detected sources that have signal-to-noise ratio of three or better to match with the flux-limit–survey-area curve shown in their Figure 19. In order to convert their 2–8 keV count rate to 2–10 keV flux, we have regenerated the ARF for an exposure-weighted average of all the CDF-N Chandra observations used by Alexander et al. (2003), assuming a $\Gamma = 1.7$ power law and using CALDB 4.5.7. Since their flux-limit–survey-area curve is based on $\Gamma = 1.4$ and old calibration, we have adjusted their curve for our flux definition.

We use the optical identifications listed in Trouille et al. (2008), which include redshifts from the literature as well as from their own program. We have further imposed a lower flux cut of $S_X > 8.9 \times 10^{-16}$ erg s^{-1} cm^{-2} to ensure an identification completeness of at least 90%, leaving 182 extragalactic X-ray point sources.

3.9. Chandra Deep Field South (CDF-S)

An extensive X-ray source and identification catalog of the 4 Ms Chandra Deep Field South was published by Xue et al. (2011), which also includes a list of previously published spectroscopic and photometric redshifts. Subsequently, Lehmer et al. (2012) generated limiting-flux–solid-angle curves and the $\log N - \log S$ relation. This work took into account flux probability distributions and recovery functions for those sources with a threshold probability of false detection of $P_{\text{thresh}} = 0.004$, as adopted by Xue et al. (2011).

We have chosen hard X-ray sources that have been detected in the 2–8 keV band from their catalog. Their count rate-to-flux conversion is based on the effective photon index Γ from the ratio of the hard- and soft-band count rates, and therefore the ECF is variable. For each source, we have converted their 2–8 keV flux (based on their estimated Γ) to the 2–10 keV flux based on $\Gamma = 1.7$, using the aim-point response matrix of one of the CDF-S observations (OBSID = 12049). As shown below, the value of the count rate-to-flux conversion factor is subject to the variation of instrumental response over time as

well as calibration updates, but the relative change of conversion factors among different spectra is insensitive to the ACIS-I response matrix used. The 2–10 keV flux (after the conversion) of the faintest object among the hard-band-detected sources was 8.3×10^{-17} erg s^{-1} cm^{-2}.

We have used the 2–8 keV band limiting-flux–solid-angle curve in Figure 2 of Lehmer et al. (2012). Their curves are drawn for $\Gamma = 1.0$, and we have converted their relation to $\Gamma = 1.7$ using the method described above.

We have further included new spectroscopic redshifts that are not included in the Xue et al. (2011) catalog. In the catalog of Xue et al. (2011), there are two objects with photometric redshifts above $z_{\text{ph}} > 7$. The second solutions of these objects by Luo et al. (2010) are both at $z_{\text{ph}} \approx 3$. However, a new spectroscopic redshift obtained for one of them (XID = 28) is $z_{\text{sp}} = 0.69$. Thus it is possible that the other also suffers a similar catastrophic photometric redshift error as well. Thus we have excluded the remaining $z_{\text{ph}} > 7$ object from our sample. The overall identification completeness is 97% (including photometric redshifts), and the spectroscopic completeness is 71%.

3.10. Removing Compton-thick AGNs

The 2–10 keV selected samples, especially at low redshifts, are highly selected against CTK AGNs. Even the Swift BAT sample selected at 15–55 keV suffers from suppression of the CTK population because of the Compton scattering itself, which results in subsequent lowering of the photon energy as well as longer paths in the absorbing medium. However, there always is some spillover of the CTK population to the sample defined here. There are two approaches in treating the situation. One is to include the CTK population into the model and make model fits to the sample that may include CTK AGNs. In other words, the amount of CTK AGN spillover is estimated by the model. The model of U14 introduced the parameter f_{CTK}, which is the ratio of the number density of the CTK AGNs ($24 \leqslant \log N_H < 26$) to that of absorbed CTN AGNs ($22 < \log N_H < 24$), and U14 then assumed the same f_{CTK} at all luminosities and redshifts. U14 showed that this is at least consistent with various observational estimates of the CTK AGN population in the literature. However, U14 also estimated that the observational constraint on this parameter was $0.5 < f_{\text{CTK}} < 1.6$, carrying a factor of three uncertainty. This is consistent with recent results by Buchner et al. (2015). An alternative approach is to remove known CTK AGNs from the sample on a best effort basis and construct an XLF model that represents only the CTN AGNs. We take the latter approach.

There are a number of studies aimed at identifying CTK AGNs among the AGN samples used in this paper. Because the Swift BAT sample is selected in the 15–55 keV band, it has some sensitivity to CTK AGNs with $\log N_H \lesssim 25$. Ajello et al. (2012) list 18 known CTK AGNs from their preceding work of Burlon et al. (2011) and other literature. These have been excluded from our analysis. Ajello et al. (2012) estimated that a few unknown CTK AGNs might still be present in this sample, the effect of which on our analysis is negligible. In their XMM-Newton Lockman Hole sample, 11 AGNs meet the X-ray color–color criteria of CTK AGNs defined by Brunner et al. (2008). None of them is in our hard-band-selected sample above our luminosity cut. Lanzuisi et al. (2015) selected 10 CTK AGNs based on spectral fits for the XMM-COSMOS sources that have 30 counts or more in the full 0.3–10 keV

band. None of them are in the *XMM* part of the XC-COSMOS AGN sample. Note that all but one of the *XMM-Newton* AGNs in the *XMM* part of the XC-COSMOS sample have 0.5–10 keV counts greater than 30; thus, Lanzuisi et al. (2015) would have identified almost all of the CTK AGNs in it, if any were present. One AGN in our CLANS sample is among the five X-ray-selected CTK AGNs given by Polletta et al. (2007), and this has been excluded from our analysis. Nine of the CDF-N AGNs are among the CTK AGN candidates derived from the X-ray spectral analysis by Georgantopoulos et al. (2009). These are also excluded from our analysis. Georgantopoulos et al. (2009) performed spectral analysis of the CDF-N AGNs with a 2–10 keV flux of $>1 \times 10^{-15}$ $\left[\mathrm{erg\ s^{-1}\ cm^{-2}}\right]$, which is approximately the same as our flux cut to the CDF-N sources to meet our completeness criteria. Recently, Brightman et al. (2014) published a table of extensive X-ray spectral analysis results of the X-ray sources in the CDF-S, AEGIS-XD, and C-COSMOS surveys with an intention to identify CTK AGNs. Because of the low background level of the *Chandra* surveys, they attempted spectral analysis to the sources down to 10 *Chandra* ACIS counts. Following the criteria by Brightman et al. (2014), we consider as probable CTK AGNs those that satisfy both of the conditions; the best-fit value of log N_{H} is greater than >24, and the lower bound of its 90% confidence error range is >23.5. We exclude these from from our analysis as well. The number of excluded sources by the CTK AGN criteria is 24 for the C-COSMOS and 23 for the CDF-S samples, respectively. The full band counts of almost all of the faintest sources above our flux cuts (see above) well exceed 10 counts for both the C-COSMOS and CDF-S samples. Thus, CTK AGNs that may still remain in our sample can be neglected. The CTK AGNs are still a minor population in our sample, even at the faint end. The CTK AGNs identified above comprise $19 \pm 6\%$, $9 \pm 3\%$, $3.6 \pm 0.5\%$, and $1.9 \pm 0.3\%$ for the log S_{X} ranges of (−16.1, −15.5), (−15.5, −15.0), (−15.0, −14.5), and (−14.5, −14.0), respectively, where the value of −16.1 corresponds to the faintest source in our sample. These fractions are consistent with the model prediction by U14 for $f_{\mathrm{CTK}} = 1$ (see Figure 17 of U14).

3.11. Sample Summary

In each sample except for *Swift* BAT, we have converted the 2–10 keV fluxes of all the sources using the ECF, assuming a power-law spectrum with a photon index of $\Gamma = 1.7$. To represent fluxes calculated in this way, we use the symbol $S_{\mathrm{X,obs}}$, or $S_{\mathrm{X,obs}}^{\Gamma=1.7}$ when we want to emphasize that we use the ECF based on $\Gamma = 1.7$. We also define the *observed luminosity*

$$L_{\mathrm{X,obs}} \equiv 4\pi d_{\mathrm{L}}(z)^2 S_{\mathrm{X,obs}}, \tag{1}$$

where $d_{\mathrm{L}}(z)$ is the luminosity distance at the redshift z. Implementation of the K-corrections and absorption corrections using realistic AGN spectra is discussed in Section 4.3. In our further analysis, we are interested in X-ray sources with intrinsic luminosities of log $L_{\mathrm{X}} > 42.0$, and we use, in effect, X-ray point sources with log $L_{\mathrm{X,obs}} \gtrsim 41.5$. Thus our analysis is strongly deselecting non-AGN X-ray sources, the number density of which is lower than AGNs by at least an order of magnitude at log $L_{\mathrm{X}} \gtrsim 41.5$ (Persic et al. 2004; Ranalli et al. 2005; Ptak et al. 2007). Our sample is plotted in the $z - \log L_{\mathrm{X,obs}}$ space in Figure 2.
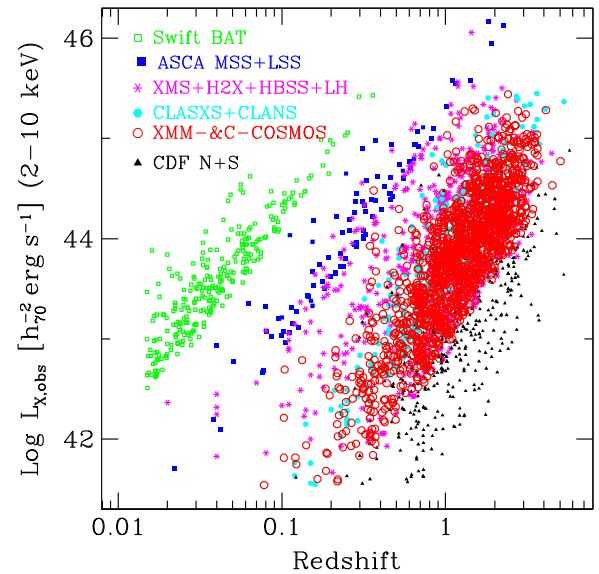

Figure 2. Sample used in our analysis in the redshift-observed X-ray luminosity space. The surveys (or a group of similar surveys) are shown in different colors/symbols, as labeled.

The properties of each sample used in our analysis is summarized in Table 1, where the name of the survey, the survey solid angle, the limiting flux corresponding to 20% of the maximum solid angle, the number of extragalactic point sources with spectroscopic redshift, those with photometric redshift, and the identification completeness are listed for each survey. The numbers in this table do not include CTK AGNs that have been discussed in the previous section nor those below our luminosity cut.

3.12. Incompleteness Correction and Number Counts

While the identification completeness of our selected samples is at least 90%, we further account for unidentified sources as follows. For samples with five or fewer unidentified sources, we have multiplied the survey area in the flux-limit–survey-area curve by the identification completeness of the sample over the whole flux range, assuming that the redshift (or the source-type) probability distribution of an unidentified source is the same as the redshift/source-type distribution of the identified sources in the same sample.

If there are more than five unidentified sources, we have made a similar adjustment of the survey area in flux blocks. We divide the X-ray sources into flux blocks from the brightest to faintest, in such a way that a new block starts after the fifth unidentified source. The last (faintest) block may contain one to five unidentified sources. For each block, we have adjusted the survey area by multiplying by the completeness level of the block. The assumption is that the redshift/source-type probability distribution is the same as that of the identified source at similar X-ray fluxes.

The resulting incompleteness-corrected limiting-flux curve of each survey, as well as that for the total of all surveys, is plotted in Figure 3(a). In order to verify the integrity and consistency of our samples and the level of systematic errors and/or the effects of cosmic variance, we plot the "tilted" cumulative number count $S_{\mathrm{X14,obs}}^{1.5} N\left(> S_{\mathrm{X}}\right)$ curves in Figure 3(b), where $S_{\mathrm{X14,obs}}$ is the 2–10 keV observed flux (see above) measured in units of $10^{-14}\mathrm{erg\ s^{-1}\ cm^{-2}}$ for each of

Table 1
The X-Ray Samples

Survey	Max. Solid Angle [deg²]	log $S_{X,obs}^{lim}$ [a] [cgs]	N_{sz} [b]	N_{pz} [c]	Completeness[d] %
Swift BAT	3.9×10^4	−11.4	274	0	98
ASCA LSS+MSS	91.	−12.5	94	0	97
HBSS	25.	−12.6	62	0	97
Hellas2XMM	3.8	−13.5	115	0	90
XMS	1.38	−13.7	128	0	91
CLANS	0.49	−14.5	183	63	90
CLASXS	0.32	−14.4	96	23	90
XC-COSMOS	2.17	−14.6	940	424	98
LH-*XMM*	0.20	−14.7	155	102	98
CDF-N	0.125	−15.5	118	54	90
CDF-S	0.128	−15.8	254	85	97

[a] The limiting flux corresponding to 20% of the maximum solid angle of each survey. The fluxes are in the 2–10 keV band.
[b] The number of extragalactic X-ray point sources with spectroscopic redshifts.
[c] The number of extragalactic X-ray point sources with photometric redshifts, but with no spectroscopic redshifts.
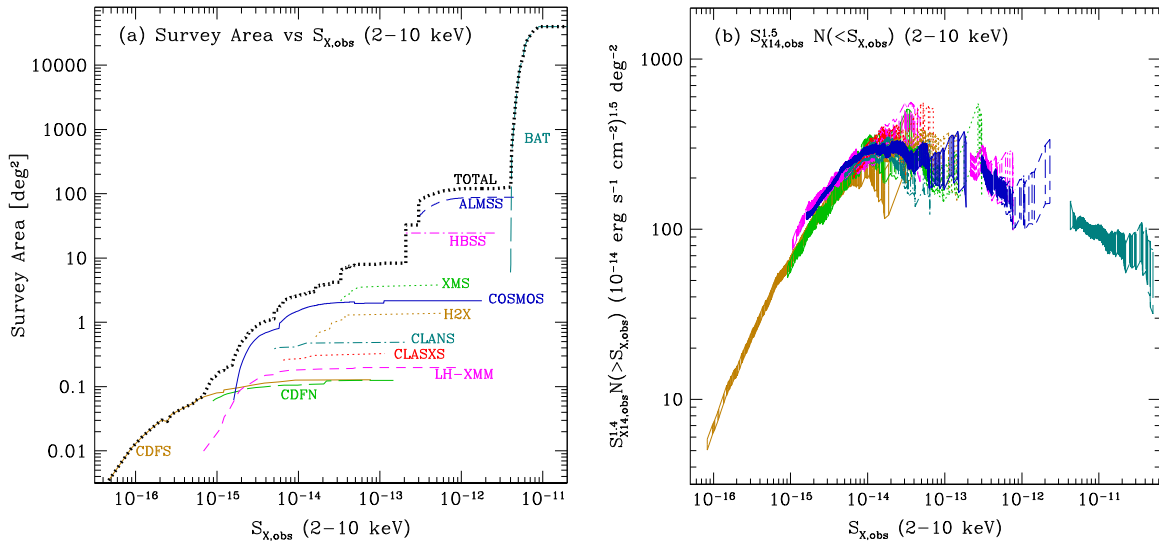[d] Identification completeness.

Figure 3. (a) Completeness-corrected survey area curve as a function of the 2–10 keV flux limit. A photon index of $\Gamma = 1.7$ is assumed for all count rate-to-flux conversions. The total area, as well as those for individual surveys, is shown as labeled. (b) The "tilted" cumulative number counts $S_{X,obs}^{1.5} N(> S_{X,obs})$ for individual samples with 1σ errors. The multiplication factor $S_{X14,obs}^{1.5}$ is applied to the cumulative number to make the Euclidean slope flat. The meaning of line colors and styles corresponds to those in the the flux-limit–survey-area curves in panel (a). For visibility, the data points corresponding to the four brightest objects in each sample are not displayed.

our identified extragalactic X-ray point source samples. The cumulative count is calculated by

$$N(> S_{X,obs}) = \sum_{S_{X,obs,i} > S_X} 1/\Omega_c(S_{X,obs,i}), \quad (2)$$

where $\Omega_c(S_{X,obs,i})$ is the corrected survey area at the limiting flux of the ith source, $S_{X,obs,i}$. One-sigma errors, calculated by

$$\sigma[N(> S_{X,obs})]^2 = \sum_{S_{X,obs,i} > S_{X,obs}} [1/\Omega_c(S_{X,obs,i})]^2, \quad (3)$$

are shown. For visibility, we do not plot data points corresponding to the four brightest object of the survey.

4. XLF CALCULATIONS

4.1. Parametric Modeling with Maximum-likelihood Fitting

We follow the same procedure as in our previous work (Miyaji et al. 2000a, 2001; Ueda et al. 2003, 2014) and determine the best-fit parameters of the parameterized model of the XLF.

As our ML estimator, we use either one of the following two forms:

$$\mathcal{L} = -2 \, \Sigma_i \ln[N(\log L_{Xi}, z_i)] + 2 \iint N(\log L_X, z) d \log L_X \, dz \quad (4)$$

$$\mathcal{L} = -2 \sum_i \ln \left[\frac{N(\log L_{Xi}, z_i)}{\iint N(\log L_X, z) d \log L_X \, dz} \right], \quad (5)$$

where i goes through each AGN in the sample and $N(\log L_X, z)$ (N-function) is the expected number density of AGNs in the sample per logarithmic luminosity per redshift, calculated from a parameterized analytic model of the XLF:

$$N(\log L_X, z)=$$
$$\frac{d\,\Phi}{d\,\log L_X}\,d_A(z)^2\,(1+z)^2\,\frac{d\chi}{dz}(z)\cdot A(S_{X,obs}), \qquad (6)$$

where $d_A(z)$ is the angular diameter distance, χ is the radial comoving distance (e.g., Section 4.3 of Schneider 2006), and $A(S_{X,obs})$ is the survey area as a function of limiting observed X-ray flux $S_{X,obs}$, as shown in Figure 3(a). For a power-law spectrum with a photon index of Γ,

$$S_{X,obs} = L_X / 4\pi d_L(z)^2 (1+z)^{2-\Gamma}, \qquad (7)$$

$d_L(z)$ is the luminosity distance.

The minimization of $\mathcal{L}$ with respect to model parameters gives the best-fit model. With Equation (5), employed in our previous works, the parameter that represents the global normalization cannot be a fitting parameter because within the estimator itself, the model number density is normalized. On the other hand, with Equation (4), employed by, e.g., Marshall et al. (1983), one can treat the normalization as a fitting parameter.

We use the MINUIT package (James 1994) distributed as a part of the CERN program library for the minimization procedure and parameter error search. The MINUIT command "MINOS" gives errors taking parameter correlations into account. In cases of global expressions (Section 5), "MINOS" fails to give errors for many parameters if we use Equation (4). In this case, we use Equation (5), and the normalization and its errors are calculated independently of the fitting process as follows. The model normalization A (as a generic symbol of various normalizations that appear in the following subsections) is determined, such that the total number of expected objects is equal to the number of AGNs in the sample (N^{obs}). The estimated 1σ confidence error for A is taken to be $A/\sqrt{N^{obs}}$ and does not include correlations of errors with other parameters. In our results, we indicate which method has been used for each fit.

4.2. Photometric Redshift Full-Probability Density Distribution

For the CLASXS, CLANS, COSMOS, LH, and *Chandra* Deep Field North and South data sets, significant fractions of redshifts rely on photometric redshift determinations. Especially for fainter optical sources, which are systematically selected against for spectroscopic measurements, the error in the primary peak and the catastrophic failure rate increase rapidly. Thus we include the PDF in redshift space for photometric redshifts, whenever available.

Let the PDF of the ith object be $p_i(z)$ (normalized with $\int p(z)dz = 1$). The X-ray luminosity of the ith object $L_{X,i}(z)$ is now a function of z. The PDFs can be incorporated into Equations (4) and (5) by replacing $N(\log L_{Xi}, z_i)$ by

$$\int N(\log L_{Xi}(z), z))p_i(z)dz. \qquad (8)$$

We use the PDFs derived by Salvato et al. (2011) and Fotopoulou et al. (2012) for the COSMOS and LH samples, respectively. They give the PDFs in bins of $\Delta z = 0.01$ in the

$0 < z < 7$ range. To reduce the computational time and at the same time not sacrifice the accuracy, we rebinned the PDFs into $\Delta z/(1+z) \approx 0.03$ bins and then neglected the new bins that have a probability of less than 2%. For the CLASXS, CLANS, and CDF samples, no PDF information was available in the public domain at the time of our analysis. However, for the CDF-S, Xue et al. (2011) show the first and second peaks of the photometric redshift PDF derived by Luo et al. (2010) for some of their photometric redshifts. For those, we assumed that the PDF is the sum of two delta functions centered at these peaks, each of which has a weight of 0.5. The effects of considering the PDFs are discussed in Section 7.1.

4.3. Using Realistic AGN Spectra

Our sample contains AGNs at various absorption levels. Thus we have considered realistic absorbed spectra in our XLF calculations, following the approach by U14 (see also Miyaji et al. 2000b; Ueda et al. 2003; Ebrero et al. 2009). In this work, we do not estimate the N_H on individual AGNs nor derive the N_H function from our own data set. Instead, we include in our model fitting the latest luminosity and redshift-dependent N_H function, $f(L_X, z; \log N_H)$, from the literature and AGN template spectrum. Ueda et al. (2014) derived the refined N_H function and its evolution, where the evolution of the absorbed AGN fraction is based on that of Hasinger (2008). Writing down the full form of the N_H function is beyond the scope of this paper, and the reader is directed to Ueda et al. (2014). The N_H function is normalized as $\int_{20}^{24} f(L_X, z; \log N_H)d\log N_H = 1$ (unabsorbed AGNs with $\log N_H < 20.0$ are included in the $20 \leqslant \log N_H < 21$ bin). At $z = 0$, the N_H function of U14, which is based on the nine month *Swift* BAT, AMSS, and SXDS surveys, is in good agreement with that of Burlon et al. (2011), which is based on the three year *Swift* BAT survey.

Additionally, U14 generated a set of sophisticated template X-ray spectra of AGNs, which include (1) an underlying power-law continuum with a high-energy cutoff at $E_c = 300$ keV; (2) a reflection component; and (3) a scattering component from the surrounding gas outside the torus, corresponding to 1%, with a torus-opening solid angle, 2π, and an intrinsic absorption with Compton-scattering derived from Monte Carlo simulations. For our purpose, we take the spectral energy distribution (SED) templates in Figure 7 of U14 for $\log N_H[\text{cm}^{-2}] = 20.5, 21.5, 22.5,$ and 23.5, but ignore the luminosity and redshift dependence of the SED. In these template spectra, $\Gamma = 1.94$ and $\Gamma = 1.84$ are assumed for the primary power-law continuum for $\log N_H[\text{cm}^{-2}] < 22$ and >22 AGNs, respectively.

In this section, we refine our definitions. The symbol L_X represents an intrinsic rest-frame 2–10 keV luminosity of the primary power law, which does not include the reflection component. This is because including the reflection component double counts the intrinsic isotropic luminosity of the AGN. The reflection component is typically $\sim 15\%$ of the primary power law in the 2–10 keV band. The symbol $d\Phi/d\log L_X$ is the comoving number density of AGNs per dex in L_X for all CTN AGNs ($\log N_H < 24.0$).

To feed realistic spectra into the ML procedure, the N function, Equation (6), should be a function of observable quantities for each sample. We define the "observed" 2–10 keV luminosity defined in Equation (1).

In this case, clearly distinguishing between observed and intrinsic X-ray luminosities, Equation (6) can be rewritten as

$$N\left(\log L_{X,\text{obs}}, z\right)d \log L_{X,\text{obs}}dz =$$

$$\int_{20}^{24} \left(\frac{d\,\Phi}{d \log L_X}d \log L_X\right) d_A(z)^2 (1+z)^2 \frac{d\chi}{dz}(z)dz$$

$$\times f\left(L_X, z; N_H\right)A\left[S_{X,\text{obs}}\left(L_X, N_H, z\right)\right]d \log N_H, \qquad (9)$$

where $S_{X,\text{obs}}$ is now a function of N_H in addition to L_X and z. The integral is over log N_H, and the intrinsic luminosity L_X is a unique function of $L_{X,\text{obs}}$, N_H, and z. The ratio of $d \log L_{X,\text{obs}}/d \log L_X$ becomes nonunity only if the spectrum changes with L_X for a given N_H, which is the case for the *Swift* BAT sample (see below).

In each template spectrum, with an intrinsic 2–10 keV luminosity of the power-law continuum L_X, we can calculate the observed luminosity at $2(1+z) - 10(1+z)$ keV ($L_{X,\text{tmp}}^{\text{obs}}(N_H, z)$). The true 2–10 keV flux from this object under this template spectrum is now

$$S_{X,\text{obs}}^{\text{tru}} = L_X/4\pi d_L(z)^2 \cdot \frac{L_{X,\text{tmp}}^{\text{obs}}(N_H, z)}{L_X}. \qquad (10)$$

The difference between $S_{X,\text{obs}}^{\text{tru}}$ to $S_{X,\text{obs}}^{\Gamma=1.7}$ (or the cataloged flux with an ECF calculated with $\Gamma = 1.7$ or our assumed spectrum for the ECF) is often neglected in the literature. In reality, it becomes important for highly absorbed AGNs (log $N_H \gtrsim 23$) at low redshifts ($z \lesssim 1$) in "2–10 keV" surveys because the effective areas of the instruments used in generating our sample other than *Swift* BAT drop rapidly as we go from 2 to 10 keV. Thus the ECF increases rapidly as the spectrum gets harder.

An ideal approach would be to use a separate response curve and count-rate–survey-area relation for each survey, as U14 did, since each survey uses different instruments and/or different observational epochs, for which the calibration may vary. However, a limitation of the software that we use for this work is that it can only accept one flux-limit–solid-angle curve, as the software is a legacy from a series of single-band soft X-ray luminosity work by Miyaji et al. (2000a, 2001) and Hasinger et al. (2005). While this reduces the accuracy of the estimate of $S_{X,\text{obs}}^{\text{tru}}$, the calculation speed gained by this simplification has allowed us to explore analytical forms for various subsets and cases (see below). We find that the relative ECFs between those for absorbed AGN spectra and for $\Gamma = 1.7$ are not very sensitive to which instrument we use. For example, the ratios of the ECFs for an extremely hard object ($\Gamma = 1.7$ with log $N_{NH} = 23.5$ at $z = 0.2$) to that for an unabsorbed $\Gamma = 1.7$ spectrum are 2.0, 2.1, and 1.7 for the *XMM-Newton* PN+2MOS (count rate at 2–8 kV), the *Chandra* ACIS-I Cycle 8 (count rate at 2–7 keV), and the *ASCA* GIS (CR at 2–10 keV), respectively. Here we use the response for ACIS-I for the conversion between $S_{X,\text{obs}}^{\text{tru}}$ to $S_{X,\text{obs}}^{\Gamma=1.7}$. A caveat is that this causes some inaccuracy for the HBSS (CR is at 4.5–7.5 keV) and *XMM-Newton* LH surveys (CR is at 2–4.5 keV). However, the impact is relatively minor because these latter surveys contain a relatively small fraction of sources in the relevant flux range, i.e., the HBSS is overwhelmed by the ASCA MSS+LSS, and the LH sample by the COSMOS sample, in their respective flux coverages.

For the *Swift* BAT sample, the selections are made using the 15–55 keV range, which is very little affected by the absorption

up to log $N_H = 24$. Despite the limitation of our software described above, the *Swift* BAT sample can be treated separately because the flux regime covered by this sample does not overlap with any other. We have made the conversion between the 2–10 keV and the 15–55 keV bands as follows.

In the comparison between *Swift* 14–194 keV and deabsorbed *MAXI* 2–10 keV luminosities, Ueda et al. (2011) pointed out that the effective power-law index between these bands varies with luminosity from $\Gamma_l = 1.7$ to $\Gamma_u = 2.0$. We have confirmed this by comparing the 14–55 keV luminosities from the Ajello et al. (2012) catalog with 4–10 keV luminosities in the latest *MAXI* catalog of Hiroi et al. (2013). To approximately represent the change, we use a smoothly varying luminosity-dependent effective spectral index

$$\Gamma_{\text{eff}} = \Gamma_l + 0.5\ \text{erf}\left[\left(\log L_X - 44.0\right)/2.0\right]\left(\Gamma_u - \Gamma_l\right) \quad (11)$$

for the conversion between the 2–10 keV and 15–55 keV fluxes, where erf is the error function. U14 hypothesize that the main cause of this slope change is the difference between type-1 and type-2 AGNs in the strength of the component reflected by the torus (i.e., the torus tends to be thicker in type-2 AGNs) in combination with the relation that the type-2 fraction decreases with luminosity. Because of the definition of L_X in this section, the 2–10 keV flux is calculated based on $(1 + 0.15)L_X$ following the assumption that 15% of intrinsic 2–10 keV luminosity is added by the reflection component. A small K-correction has been made based on Γ_{eff}. In order to use our flux-limit–survey-area curve, we have back-converted from the 15–55 keV flux to the observed flux $S_{X,\text{obs}}^{\Gamma=1.7}$, using our reference slope $\Gamma = 1.7$.

As a technical note, we comment that U14 chose to use the count rate as an independent variable to the *N*-function instead of log $L_{X,\text{obs}}$.

4.4. $N_{\text{obs}}/N_{\text{mdl}}$ Method for the Binned XLF

A less biased way of presenting the binned XLF than the classical $\sum 1/V_a$ (Avni & Bahcall 1980) is the $N_{\text{obs}}/N_{\text{mdl}}$ estimator described in Miyaji et al. (2001; see also La Franca & Cristiani 1997). The basic procedure is as follows.

1. Divide the combined sample into several redshift shells. For each redshift shell, fit the AGN XLF with a smooth analytical function obtained with the ML fit as described above.
2. For each redshift shell, count the number of objects that fall into each luminosity bin to obtain the observed number of objects (N_{obs}).
3. For each luminosity bin, evaluate the analytical fit at the central luminosity/redshift ($d\Phi^{\text{mdl}}/d \log L_X$).
4. Calculate the predicted number of AGNs in the bin (N_{mdl}).
5. The final result is

$$\frac{d\Phi}{d \log L_X} = \frac{d\Phi^{\text{mdl}}}{d \log L_X} \cdot N_{\text{obs}}/N_{\text{mdl}}. \qquad (12)$$

We note that in the case that the XLF model is constant within the bin, the $N_{\text{obs}}/N_{\text{mdl}}$ estimator is mathematically equivalent to that proposed by Page & Carrera (2000). In the case of taking absorption into account with the method described above in Section 4.3, and binning by log L_X defined

there, deriving N_{obs} is not straightforward because we cannot determine log L_X individually from single-band fluxes. The N_H values derived from hardness ratios are subject to large errors and not necessarily available for all objects in the sample. On the other hand, it is straightforward to calculate from the model probability distribution of N_H for given redshift and observed flux: $p(z, S_{X,obs}; \log N_H)$, which can be normalized as

$$\int_{20}^{24} p(z, S_{X,obs}; \log N_H) d \log N_H = 1. \qquad (13)$$

This is different from the N_H function $f(L_X, z; \log N_H)$, which is the distribution of N_H for given redshift and intrinsic luminosity. For our purpose, for the ith object with a given $(z_i, S_{X,obs,i})$, we use the probability distribution of the intrinsic luminosity:

$$p_i\left(\log L_X\left[(z_i, S_{X,obs,i}, N_H)\right]\right) d \log L_X = $$
$$p(z_i, S_{X,obs,i}; \log N_H) d \log N_H. \qquad (14)$$

If we would like to calculate N_{obs} in the redshift-intrinsic luminosity bin $(z_1, z_2; \log L_1, \log L_2)$:

$$N_{obs} = \sum_i \int_{\log L_1}^{\log L_2} p_i(\log L_X) d \log L_X, \qquad (15)$$

where i is over objects with redshifts between z_1 and z_2. In practice, we calculate N_{obs} as weighted sums over log $N_H = 20.5, 21.5, 22.5,$ and 23.5 templates. Similarly, we include the PDFs of photometric redshifts into N_{obs} estimations by adding the portion of the PDF of each objects that falls into the redshift bin, as has been made also by Aird et al. (2010).

One limitation is that the errors assuming Poisson statistics are not valid if N_{obs} is a sum of weights, unlike the cases of our previous works (Miyaji et al. 2001; Hasinger et al. 2005; U14), in which N_{obs} were always integers. However, we use the approximate 1σ Poisson errors from the Gehrels (1986) Equations (7) and (12) ($S = 1$) for the upper and lower 1σ errors, respectively. Thus, the errors are only approximate. Additionally, the errors in different bins are not independent of one another.

5. GLOBAL XLF EXPRESSION

5.1. Luminosity-dependent Density Evolution Model

For the analytical expression of the XLF at $z = 0$, we use the smoothed two-power-law formula.

$$\frac{d \Phi(L_X, 0)}{d \log L_X} = A_{44}^{z=0} \frac{\left(\frac{10^{44}}{L_{x,*}}\right)^{\gamma_1} + \left(\frac{10^{44}}{L_{x,*}}\right)^{\gamma_2}}{\left(\frac{L_X}{L_{x,*}}\right)^{\gamma_1} + \left(\frac{L_X}{L_{x,*}}\right)^{\gamma_2}}$$
$$\equiv \frac{A_*^{z=0}}{\left(\frac{L_X}{L_{x,*}}\right)^{\gamma_1} + \left(\frac{L_X}{L_{x,*}}\right)^{\gamma_2}}. \qquad (16)$$

The normalization $A_{44}^{z=0}$ is the XLF value at $(\log L_X, z) = (44, 0)$. There is also a convention to use A_* (second line in Equation (16)) as a normalization parameter. We primarily use $A_{44}^{z=0}$ because A_* is strongly coupled with the break luminosity $L_{X,*}$, and therefore it is not possible to

estimate its error accurately with our ML-fitting procedure (see below).

Following the most successful analytical form of the evolution in the literature, we use the LDDE:

$$\frac{d\Phi(L_X, z)}{d \log L_X} = \frac{d\Phi(L_X, 0)}{d \log L_X} \cdot e_d(z, L_X), \qquad (17)$$

where $e_d(z, L_X)$ is the density evolution factor normalized to $z = 0$. We describe it with a three-segment power-law model:

$$e_d(z, L_X) = \begin{cases} (1 + z)^{p_1} & (z < z_{b1}) \\ e_d(z_{b1}, L_X) \cdot \left(\frac{1+z}{1+z_{b1}}\right)^{p_2} & (z_{b1} \leqslant z < z_{b2}) \\ e_d(z_{b2}, L_X) \cdot \left(\frac{1+z}{1+z_{b2}}\right)^{p_3} & (z \geqslant z_{b2}). \end{cases} \qquad (18)$$

As in the previous works, the first-break positions z_{p1} may depend on luminosity at the low-luminosity regime:

$$z_{b1}(L_X) = \begin{cases} z_{b,0}(L_X/L_{x,b})^\alpha & (L_X \leqslant L_{x,b}) \\ z_{b,0} & (L_X > L_{x,b}) \end{cases}. \qquad (19)$$

We also include the luminosity dependence of the evolution indices $p1$ and $p2$:

$$p_1(L_X) = p_{1,44} + \beta_1 (\log L_X - 44) \qquad (20)$$

$$p_2(L_X) = p_{2,44} + \beta_2 (\log L_X - 44). \qquad (21)$$

5.2. Global LDDE Results

The best-fit parameters of our LDDE model and 1σ errors, corresponding to $\Delta\mathcal{L} = 1$, are shown in Table 2. For the global expression, the fits using the likelihood function, Equation (5), give much more stable error search results than those using Equation (4). As stated above, minimizing in Equation (5) cannot determine the normalization. Thus the $A_{44}^{z=0}$ value and its error are determined by scaling it such that it gives the total number of objects (N_{tot}) for best-fit values of other parameters. The fractional error of $1/\sqrt{N_{tot}}$ is used for its error. Thus the errors of $A_{44}^{z=0}$ in Table 2 do not contain correlation of errors with other parameters. The traditional normalization $A_*^{z=0}$ (see Equation (16)) is also shown without an error for reference.

The parameters for the fit in which the realistic AGN spectra, N_H function (Section 4.3), and the PDFs of photometric redshifts (Section 4.2) are fully taken into account are listed under "Full" in Table 2. For our final results, we show the case where $z_{b1,44}$ is fixed to 1.1 and $z_{b1,44} = 2.7$ because fitting with all parameters free causes failures in the minimization processes. The values of these fixed parameters have been decided based on the results of the fits in luminosity-class-divided samples, which is explained later in Section 6.2. Since the fits in each luminosity class also use information on the global expression, the process has thus been iterative; that is, we decide on fixed parameters of the global expression, referring to the results of the luminosity-class-divided sample based on the global expression in the previous step.

Table 2
Best-fit LDDE Parameters for Global Expressions

Parameter[a]	Full	No pz-PDZ	$\Gamma = 1.8$
	$z = 0$ XLF Parameters[b]		
$A_{44}^{z=0\,c}$	$(9.3 \pm 0.2) \times 10^{-7}$	$(8.7 \pm 0.2) \times 10^{-7}$	$(9.7 \pm 0.2) \times 10^{-7}$
$A_*^{z=0\,d}$	1.56×10^{-6}	1.34×10^{-6}	1.60×10^{-6}
$\log L_{X,*}$	44.04 ± 0.08	44.06 ± 0.06	44.05 ± 0.06
γ_1	1.17 ± 0.05	1.17 ± 0.05	1.09 ± 0.04
γ_2	$2.80^{+0.16}_{-0.10}$	$2.90^{+0.08}_{-0.12}$	2.76 ± 0.08
	Evolution Parameters[b]		
$p_{1,44}$	5.29 ± 0.11	5.35 ± 0.11	4.86 ± 0.11
$z_{b1,44}$	$1.1*$	$1.1*$	$1.1*$
$p_{2,44}$	-0.35 ± 0.14	0.02 ± 0.13	0.02 ± 0.14
z_{b2}	$2.7*$	$2.7*$	$2.7*$
$p3_{44}$	$-5.6*$	$-5.6*$	$-5.6*$
α	$0.18 \pm .03$	$0.16^{+.04}_{-.01}$	$0.11^{+.01}_{-.02}$
$\log L_{x,b}$	$44.5*$	$44.5*$	$44.5*$
β_1	$1.2^{+0.3}_{-0.2}$	$1.2^{+0.2}_{-0.3}$	1.6 ± 0.2
β_2	$1.5^{+0.5}_{-0.3}$	$2.0^{+0.2}_{-0.4}$	1.7 ± 0.2

[a] Parameters that have been fixed during the fit are labeled by "(*)." Units—A (with any subscripts and superscripts): h_{70}^3 Mpc^{-3}dex^{-1}, L (with any subscripts and superscripts): h_{70}^{-2}erg s^{-1}.
[b] The 68% confidence range for one parameter ($\Delta\mathcal{L} < 1$) with correlations among parameter errors, except for $A_{44}^{z=0}$.
[c] The 1σ errors of $A_{44}^{z=0}$ are for all other parameters fixed.
[d] The traditional normalization defined as twice of the XLF value at the break luminosity at $z = 0$ ($L_{X,*}$).

6. XLFs IN REDSHIFT SHELLS AND LUMINOSITY CLASSES

6.1. Adaptive Binning

In this section, we present the binned XLF, as well as the analytical formula of the XLF divided into redshift shells. We also present the number density curve divided in luminosity classes. The binning has been decided on an adaptive basis, so that the sizes of the error bars and bin sizes are optimal for the plots to be visible and informative.

First, we divide the sample into 11 redshift shells in the same way as those used by U14, except that the two highest-redshift shells by U14 ($z > 3.0$) are combined into a single one for obtaining a sufficient number of objects for a separate two-power-law fit. For each redshift shell, we construct luminosity bins such that each contains 20 objects by default, with minimum and maximum bin sizes of $\Delta \log L_X = 0.125$ and 0.5, respectively. In case the most luminous bin contains less than 20 objects, the border between the last two bins is adjusted to contain approximately equal numbers of objects within the bin-size constraints.

For the luminosity division, the range $42.0 \leqslant \log L_X \leqslant 46.0$ is divided into four $\Delta \log L_X = 1.0$ classes. Each luminosity class is divided into redshift bins such that each bin has 20 objects (using the best-fit photometric redshifts for those without spectroscopic redshift) with forced minimum and maximum sizes of $\Delta \ln (1 + z) = 0.07$ and 0.5, respectively. If the highest-redshift bin has less than 20 objects, the border between the highest two redshift bins is adjusted in the same way as in the case of luminosity binning. Due to the small number of objects, the default number of objects per redshift bin for the $45.0 \leqslant \log L_X \leqslant 46.0$ class has been set to 7, with the same minimum and maximum bin-size constraints.

6.2. Analytical Form for Each Redshift Shell

For the analytical expression of the XLF in each redshift shell, we use the *smoothed two-power-law* formula. Because the redshift shells have finite widths, the fit results depend on the evolution of the SXLF within them:

$$\frac{d\,\Phi(L_X, z)}{d\,\log L_X} = A_{44}^z \frac{\left(\frac{10^{44}}{L_{x,*}}\right)^{\gamma_1} + \left(\frac{10^{44}}{L_{x,*}}\right)^{\gamma_2}}{\left(\frac{L_X}{L_{x,*}}\right)^{\gamma_1} + \left(\frac{L_X}{L_{x,*}}\right)^{\gamma_2}} \times e_d(z, L_X), \quad (22)$$

where $e_d(z, L_X)$ is the density evolution factor. While the final results are insensitive to the detailed behavior of $e_d(z, L_X)$ within the shell at most locations in the (L_X, z) space, we have taken our best estimate by using the LDDE model derived

Table 3
Smoothed 2PL Parameters for Each Redshift Shell

z-range	z_c	$A_{44}^{z=z_c}$ [a][b]	$A_*^{z=z_c}$ [a][b]	$\log L_*^{z=z_c}$ [b]	γ_1 [a]	γ_2 [a]
0.015–0.200	0.104	$1.20^{+0.14}_{-0.13} \times 10^{-6}$	8.97×10^{-6}	$43.70^{+0.18}_{-0.19}$	$0.90^{+0.14}_{-0.17}$	$2.53^{+0.23}_{-0.19}$
0.200–0.400	0.296	$4.79^{+0.65}_{-0.61} \times 10^{-6}$	3.91×10^{-6}	$44.22^{+0.21}_{-0.21}$	$1.05^{+0.08}_{-0.10}$	$2.90^{+0.37}_{-0.27}$
0.400–0.600	0.497	$7.64^{+1.53}_{-1.38} \times 10^{-6}$	1.67×10^{-5}	$43.98^{+0.20}_{-0.23}$	$0.83^{+0.11}_{-0.14}$	$2.70^{+0.48}_{-0.32}$
0.600–0.800	0.697	$1.14^{+0.17}_{-0.14} \times 10^{-5}$	2.36×10^{-4}	$43.31^{+0.29}_{-0.24}$	$0.41^{+0.24}_{-0.30}$	$1.86^{+0.17}_{-0.13}$
0.800–1.000	0.897	$3.12^{+0.37}_{-0.35} \times 10^{-5}$	8.91×10^{-5}	$43.90^{+0.13}_{-0.13}$	$0.40^{+0.13}_{-0.15}$	$2.51^{+0.27}_{-0.22}$
1.000–1.200	1.098	$3.47^{+0.35}_{-0.33} \times 10^{-5}$	1.06×10^{-4}	$43.85^{+0.14}_{-0.14}$	$0.19^{+0.16}_{-0.19}$	$2.06^{+0.18}_{-0.15}$
1.200–1.600	1.392	$4.42^{+0.31}_{-0.29} \times 10^{-5}$	3.04×10^{-5}	$44.43^{+0.09}_{-0.10}$	$0.47^{+0.07}_{-0.08}$	$2.82^{+0.32}_{-0.27}$
1.600–2.000	1.793	$3.68^{+0.32}_{-0.29} \times 10^{-5}$	2.07×10^{-5}	$44.57^{+0.10}_{-0.11}$	$0.48^{+0.09}_{-0.10}$	$2.73^{+0.38}_{-0.32}$
2.000–2.400	2.194	$4.27^{+0.50}_{-0.43} \times 10^{-5}$	3.28×10^{-5}	$44.50^{+0.12}_{-0.13}$	$0.27^{+0.14}_{-0.17}$	$2.84^{+0.52}_{-0.41}$
2.400–3.000	2.688	$3.28^{+0.48}_{-0.33} \times 10^{-5}$	1.71×10^{-5}	$44.63^{+0.09}_{-0.17}$	$0.46^{+0.12}_{-0.17}$	$3.12^{+\infty}_{-0.60}$
3.000–5.800	4.215	$4.37^{+0.90}_{-0.62} \times 10^{-6}$	1.08×10^{-6}	$44.94^{+0.20}_{-0.28}$	$0.65^{+0.19}_{-0.25}$	$4.38^{+\infty}_{-1.69}$

[a] Errors show the 68% confidence range for one parameter ($\Delta\mathcal{L} < 1$).
[b] Units—A (with any subscripts/superscripts): $[h_{70}^3$ Mpc^{-3}dex$^{-1}]$, L (with any subscripts/superscripts): $\left[h_{70}^{-2}$erg s$^{-1} \right]$.

Table 4
Full Binned XLF Divided in Redshift Shells

z-range	z_c	log L_X-range[a]	log $L_{X,c}$[a]	N_{obj}	$\frac{d\Phi}{d\log L_X}$ [a,b]
0.015–0.200	0.104	42.13–42.48	42.31	11.4	$(1.24 \pm 0.24) \times 10^{-4}$
0.015–0.200	0.104	42.48–42.61	42.54	5.2	$(5.85 \pm 1.76) \times 10^{-5}$
0.015–0.200	0.104	42.61–42.73	42.67	15.9	$(1.02 \pm 0.23) \times 10^{-4}$
0.015–0.200	0.104	42.73–42.86	42.79	16.1	$(5.58 \pm 1.28) \times 10^{-5}$
0.015–0.200	0.104	42.86–42.98	42.92	20.0	$(4.68 \pm 0.89) \times 10^{-5}$
0.015–0.200	0.104	42.98–43.11	43.04	26.1	$(3.61 \pm 0.65) \times 10^{-5}$
0.015–0.200	0.104	43.11–43.23	43.17	26.4	$(2.54 \pm 0.46) \times 10^{-5}$
0.015–0.200	0.104	43.23–43.36	43.29	26.6	$(1.54 \pm 0.26) \times 10^{-5}$
0.015–0.200	0.104	43.36–43.48	43.42	28.7	$(1.20 \pm 0.20) \times 10^{-5}$
0.015–0.200	0.104	43.48–43.61	43.54	29.6	$(7.81 \pm 1.33) \times 10^{-6}$
0.015–0.200	0.104	43.61–43.73	43.67	28.2	$(5.55 \pm 1.00) \times 10^{-6}$
0.015–0.200	0.104	43.73–43.86	43.79	14.8	$(1.85 \pm 0.46) \times 10^{-6}$
0.015–0.200	0.104	43.86–43.98	43.92	24.4	$(2.25 \pm 0.45) \times 10^{-6}$
0.015–0.200	0.104	43.98–44.11	44.04	18.9	$(1.08 \pm 0.25) \times 10^{-6}$
0.015–0.200	0.104	44.11–44.23	44.17	12.5	$(5.18 \pm 1.45) \times 10^{-7}$
0.015–0.200	0.104	44.23–44.42	44.32	9.2	$(1.44 \pm 0.48) \times 10^{-7}$
0.015–0.200	0.104	44.42–44.55	44.49	10.0	$(1.34 \pm 0.43) \times 10^{-7}$
0.015–0.200	0.104	44.55–44.70	44.63	11.0	$(7.88 \pm 2.36) \times 10^{-8}$
0.015–0.200	0.104	44.70–45.10	44.90	7.0	$(7.51 \pm 2.85) \times 10^{-9}$
0.015–0.200	0.104	45.10–45.35	45.22	2.0	$(2.53 \pm 1.77) \times 10^{-9}$
0.200–0.400	0.296	41.89–42.07	41.98	5.9	$(2.48 \pm 0.62) \times 10^{-4}$
0.200–0.400	0.296	42.07–42.30	42.18	18.4	$(3.50 \pm 0.53) \times 10^{-4}$
0.200–0.400	0.296	42.30–42.42	42.36	13.3	$(3.11 \pm 0.53) \times 10^{-4}$
0.200–0.400	0.296	42.42–42.55	42.49	12.7	$(2.03 \pm 0.35) \times 10^{-4}$
0.200–0.400	0.296	42.55–42.67	42.61	16.8	$(2.21 \pm 0.33) \times 10^{-4}$
0.200–0.400	0.296	42.67–42.80	42.74	14.3	$(1.36 \pm 0.20) \times 10^{-4}$
0.200–0.400	0.296	42.80–42.92	42.86	12.2	$(9.95 \pm 1.59) \times 10^{-5}$
0.200–0.400	0.296	42.92–43.05	42.99	10.1	$(6.07 \pm 1.03) \times 10^{-5}$
0.200–0.400	0.296	43.05–43.17	43.11	15.0	$(7.75 \pm 1.08) \times 10^{-5}$
0.200–0.400	0.296	43.17–43.30	43.24	11.7	$(4.67 \pm 0.75) \times 10^{-5}$
0.200–0.400	0.296	43.30–43.48	43.39	13.5	$(3.17 \pm 0.48) \times 10^{-5}$
0.200–0.400	0.296	43.48–43.60	43.54	4.9	$(1.25 \pm 0.33) \times 10^{-5}$
0.200–0.400	0.296	43.60–43.80	43.70	12.1	$(1.08 \pm 0.18) \times 10^{-5}$
0.200–0.400	0.296	43.80–43.92	43.86	8.4	$(6.79 \pm 1.56) \times 10^{-6}$
0.200–0.400	0.296	43.92–44.05	43.99	11.4	$(5.31 \pm 1.12) \times 10^{-6}$
0.200–0.400	0.296	44.05–44.23	44.14	11.2	$(2.49 \pm 0.52) \times 10^{-6}$
0.200–0.400	0.296	44.23–44.51	44.37	9.8	$(1.01 \pm 0.24) \times 10^{-6}$
0.200–0.400	0.296	44.51–45.01	44.76	4.3	$(1.28 \pm 0.51) \times 10^{-7}$
0.200–0.400	0.296	45.01–45.16	45.08	1.1	$(9.41 \pm 8.85) \times 10^{-9}$
0.200–0.400	0.296	45.16–45.56	45.36	2.0	$(1.28 \pm 0.90) \times 10^{-9}$
0.200–0.400	0.296	45.56–45.81	45.69	2.0	$(5.77 \pm 4.04) \times 10^{-10}$
0.400–0.600	0.497	41.90–42.19	42.04	5.9	$(2.92 \pm 0.70) \times 10^{-4}$
0.400–0.600	0.497	42.19–42.31	42.25	6.3	$(3.58 \pm 0.86) \times 10^{-4}$
0.400–0.600	0.497	42.31–42.46	42.39	10.5	$(2.96 \pm 0.56) \times 10^{-4}$
0.400–0.600	0.497	42.46–42.59	42.53	9.8	$(1.96 \pm 0.39) \times 10^{-4}$
0.400–0.600	0.497	42.59–42.71	42.65	15.3	$(2.29 \pm 0.34) \times 10^{-4}$
0.400–0.600	0.497	42.71–42.85	42.78	22.1	$(1.95 \pm 0.23) \times 10^{-4}$
0.400–0.600	0.497	42.85–42.98	42.92	22.7	$(1.53 \pm 0.18) \times 10^{-4}$
0.400–0.600	0.497	42.98–43.10	43.04	17.0	$(9.81 \pm 1.28) \times 10^{-5}$
0.400–0.600	0.497	43.10–43.23	43.17	17.3	$(7.55 \pm 0.98) \times 10^{-5}$
0.400–0.600	0.497	43.23–43.35	43.29	18.0	$(6.69 \pm 0.87) \times 10^{-5}$
0.400–0.600	0.497	43.35–43.48	43.42	16.7	$(4.45 \pm 0.58) \times 10^{-5}$
0.400–0.600	0.497	43.48–43.60	43.54	12.7	$(2.85 \pm 0.43) \times 10^{-5}$
0.400–0.600	0.497	43.60–43.73	43.67	11.8	$(2.08 \pm 0.33) \times 10^{-5}$
0.400–0.600	0.497	43.73–43.88	43.81	11.8	$(1.60 \pm 0.27) \times 10^{-5}$
0.400–0.600	0.497	43.88–44.25	44.07	13.2	$(4.79 \pm 0.77) \times 10^{-6}$
0.400–0.600	0.497	44.25–44.41	44.33	7.9	$(2.02 \pm 0.55) \times 10^{-6}$
0.400–0.600	0.497	44.41–44.53	44.47	6.5	$(1.25 \pm 0.39) \times 10^{-6}$
0.400–0.600	0.497	44.53–44.77	44.65	2.3	$(1.42 \pm 0.54) \times 10^{-7}$
0.400–0.600	0.497	44.77–45.13	44.95	2.1	$(6.14 \pm 3.50) \times 10^{-8}$
0.600–0.800	0.697	41.88–42.36	42.12	10.9	$(4.06 \pm 0.69) \times 10^{-4}$

13

Table 4
(Continued)

z-range	z_c	log L_X-range[a]	log $L_{X,c}$[a]	N_{obj}	$\frac{d\Phi}{d\log L_X}$[a,b]
0.600–0.800	0.697	42.36–42.48	42.42	6.3	$(3.83 \pm 0.84) \times 10^{-4}$
0.600–0.800	0.697	42.48–42.61	42.54	11.8	$(4.05 \pm 0.69) \times 10^{-4}$
0.600–0.800	0.697	42.61–42.73	42.67	18.4	$(4.20 \pm 0.55) \times 10^{-4}$
0.600–0.800	0.697	42.73–42.86	42.79	20.9	$(2.99 \pm 0.39) \times 10^{-4}$
0.600–0.800	0.697	42.86–42.98	42.92	29.1	$(3.26 \pm 0.33) \times 10^{-4}$
0.600–0.800	0.697	42.98–43.11	43.04	29.0	$(1.96 \pm 0.20) \times 10^{-4}$
0.600–0.800	0.697	43.11–43.23	43.17	36.7	$(1.83 \pm 0.17) \times 10^{-4}$
0.600–0.800	0.697	43.23–43.36	43.29	30.1	$(1.08 \pm 0.11) \times 10^{-4}$
0.600–0.800	0.697	43.36–43.48	43.42	30.5	$(9.83 \pm 0.95) \times 10^{-5}$
0.600–0.800	0.697	43.48–43.61	43.54	21.1	$(5.09 \pm 0.56) \times 10^{-5}$
0.600–0.800	0.697	43.61–43.73	43.67	23.0	$(4.68 \pm 0.51) \times 10^{-5}$
0.600–0.800	0.697	43.73–43.86	43.79	14.3	$(2.08 \pm 0.29) \times 10^{-5}$
0.600–0.800	0.697	43.86–43.98	43.92	13.3	$(1.68 \pm 0.25) \times 10^{-5}$
0.600–0.800	0.697	43.98–44.13	44.06	9.5	$(8.32 \pm 1.58) \times 10^{-6}$
0.600–0.800	0.697	44.13–44.52	44.33	12.5	$(3.20 \pm 0.54) \times 10^{-6}$
0.600–0.800	0.697	44.52–44.65	44.58	5.0	$(1.52 \pm 0.53) \times 10^{-6}$
0.600–0.800	0.697	44.65–45.08	44.87	15.5	$(4.40 \pm 0.88) \times 10^{-7}$
0.600–0.800	0.697	45.08–45.33	45.21	0.2	$(7.45 \pm 2.46) \times 10^{-9}$
0.800–1.000	0.897	41.98–42.48	42.23	3.9	$(1.49 \pm 0.43) \times 10^{-4}$
0.800–1.000	0.897	42.48–42.73	42.60	12.8	$(3.40 \pm 0.51) \times 10^{-4}$
0.800–1.000	0.897	42.73–42.85	42.79	11.5	$(3.13 \pm 0.47) \times 10^{-4}$
0.800–1.000	0.897	42.85–42.98	42.92	15.5	$(2.27 \pm 0.27) \times 10^{-4}$
0.800–1.000	0.897	42.98–43.10	43.04	22.2	$(2.36 \pm 0.26) \times 10^{-4}$
0.800–1.000	0.897	43.10–43.23	43.17	25.3	$(1.75 \pm 0.19) \times 10^{-4}$
0.800–1.000	0.897	43.23–43.35	43.29	25.4	$(1.26 \pm 0.13) \times 10^{-4}$
0.800–1.000	0.897	43.35–43.48	43.42	41.2	$(1.39 \pm 0.11) \times 10^{-4}$
0.800–1.000	0.897	43.48–43.60	43.54	39.3	$(1.20 \pm 0.10) \times 10^{-4}$
0.800–1.000	0.897	43.60–43.73	43.67	39.0	$(8.68 \pm 0.74) \times 10^{-5}$
0.800–1.000	0.897	43.73–43.85	43.79	28.5	$(5.37 \pm 0.54) \times 10^{-5}$
0.800–1.000	0.897	43.85–43.98	43.92	28.2	$(3.97 \pm 0.40) \times 10^{-5}$
0.800–1.000	0.897	43.98–44.10	44.04	16.5	$(1.93 \pm 0.25) \times 10^{-5}$
0.800–1.000	0.897	44.10–44.23	44.17	19.7	$(1.69 \pm 0.22) \times 10^{-5}$
0.800–1.000	0.897	44.23–44.48	44.35	18.3	$(6.69 \pm 0.94) \times 10^{-6}$
0.800–1.000	0.897	44.48–44.88	44.68	10.5	$(1.50 \pm 0.33) \times 10^{-6}$
0.800–1.000	0.897	44.88–45.13	45.01	1.3	$(6.39 \pm 3.90) \times 10^{-8}$
1.000–1.200	1.098	41.86–42.36	42.11	1.8	$(1.14 \pm 0.42) \times 10^{-4}$
1.000–1.200	1.098	42.36–42.85	42.60	11.1	$(2.15 \pm 0.37) \times 10^{-4}$
1.000–1.200	1.098	42.85–42.98	42.92	6.4	$(1.76 \pm 0.35) \times 10^{-4}$
1.000–1.200	1.098	42.98–43.10	43.04	10.4	$(1.80 \pm 0.29) \times 10^{-4}$
1.000–1.200	1.098	43.10–43.23	43.17	14.2	$(1.37 \pm 0.18) \times 10^{-4}$
1.000–1.200	1.098	43.23–43.35	43.29	14.9	$(1.12 \pm 0.15) \times 10^{-4}$
1.000–1.200	1.098	43.35–43.48	43.42	22.7	$(1.04 \pm 0.11) \times 10^{-4}$
1.000–1.200	1.098	43.48–43.60	43.54	30.4	$(1.02 \pm 0.09) \times 10^{-4}$
1.000–1.200	1.098	43.60–43.73	43.67	31.3	$(7.51 \pm 0.68) \times 10^{-5}$
1.000–1.200	1.098	43.73–43.85	43.79	30.3	$(6.65 \pm 0.63) \times 10^{-5}$
1.000–1.200	1.098	43.85–43.98	43.92	27.6	$(4.53 \pm 0.45) \times 10^{-5}$
1.000–1.200	1.098	43.98–44.10	44.04	24.6	$(3.66 \pm 0.40) \times 10^{-5}$
1.000–1.200	1.098	44.10–44.23	44.17	16.7	$(1.77 \pm 0.23) \times 10^{-5}$
1.000–1.200	1.098	44.23–44.35	44.29	12.6	$(1.07 \pm 0.17) \times 10^{-5}$
1.000–1.200	1.098	44.35–44.57	44.46	11.8	$(4.37 \pm 0.74) \times 10^{-6}$
1.000–1.200	1.098	44.57–44.98	44.78	11.4	$(1.69 \pm 0.34) \times 10^{-6}$
1.000–1.200	1.098	44.98–45.34	45.16	4.3	$(1.53 \pm 0.58) \times 10^{-7}$
1.000–1.200	1.098	45.34–45.59	45.47	4.0	$(8.73 \pm 3.75) \times 10^{-8}$
1.200–1.600	1.392	42.10–42.60	42.35	7.0	$(1.82 \pm 0.40) \times 10^{-4}$
1.200–1.600	1.392	42.60–42.86	42.73	6.3	$(1.34 \pm 0.31) \times 10^{-4}$
1.200–1.600	1.392	42.86–43.04	42.95	6.7	$(1.10 \pm 0.24) \times 10^{-4}$
1.200–1.600	1.392	43.04–43.16	43.10	10.6	$(1.53 \pm 0.26) \times 10^{-4}$
1.200–1.600	1.392	43.16–43.29	43.22	14.9	$(1.15 \pm 0.15) \times 10^{-4}$
1.200–1.600	1.392	43.29–43.41	43.35	23.1	$(1.17 \pm 0.13) \times 10^{-4}$
1.200–1.600	1.392	43.41–43.54	43.47	26.9	$(8.54 \pm 0.74) \times 10^{-5}$
1.200–1.600	1.392	43.54–43.66	43.60	37.6	$(8.73 \pm 0.71) \times 10^{-5}$

Table 4
(Continued)

z-range	z_c	$\log L_X$-range[a]	$\log L_{X,c}$[a]	N_{obj}	$\frac{d\Phi}{d \log L_X}$[a,b]
1.200–1.600	1.392	43.66–43.79	43.72	49.2	$(7.16 \pm 0.49) \times 10^{-5}$
1.200–1.600	1.392	43.79–43.91	43.85	50.6	$(5.98 \pm 0.41) \times 10^{-5}$
1.200–1.600	1.392	43.91–44.04	43.97	58.3	$(5.17 \pm 0.34) \times 10^{-5}$
1.200–1.600	1.392	44.04–44.16	44.10	44.0	$(3.40 \pm 0.26) \times 10^{-5}$
1.200–1.600	1.392	44.16–44.29	44.22	39.1	$(2.31 \pm 0.19) \times 10^{-5}$
1.200–1.600	1.392	44.29–44.41	44.35	38.2	$(2.04 \pm 0.18) \times 10^{-5}$
1.200–1.600	1.392	44.41–44.54	44.47	25.8	$(1.03 \pm 0.11) \times 10^{-5}$
1.200–1.600	1.392	44.54–44.66	44.60	23.7	$(8.19 \pm 1.06) \times 10^{-6}$
1.200–1.600	1.392	44.66–44.98	44.82	21.9	$(2.17 \pm 0.26) \times 10^{-6}$
1.200–1.600	1.392	44.98–45.10	45.04	2.0	$(4.94 \pm 2.03) \times 10^{-7}$
1.200–1.600	1.392	45.10–45.29	45.19	4.2	$(3.90 \pm 1.44) \times 10^{-7}$
1.200–1.600	1.392	45.29–45.78	45.53	2.2	$(1.48 \pm 0.77) \times 10^{-8}$
1.200–1.600	1.392	45.78–46.03	45.90	1.0	$(7.86 \pm 7.00) \times 10^{-9}$
1.600–2.000	1.793	41.91–42.41	42.16	1.3	$(1.45 \pm 0.62) \times 10^{-4}$
1.600–2.000	1.793	42.41–42.91	42.66	7.3	$(1.38 \pm 0.30) \times 10^{-4}$
1.600–2.000	1.793	42.91–43.21	43.06	8.0	$(1.05 \pm 0.22) \times 10^{-4}$
1.600–2.000	1.793	43.21–43.38	43.29	6.5	$(7.14 \pm 1.71) \times 10^{-5}$
1.600–2.000	1.793	43.38–43.51	43.44	9.2	$(6.95 \pm 1.11) \times 10^{-5}$
1.600–2.000	1.793	43.51–43.63	43.57	14.8	$(7.12 \pm 0.85) \times 10^{-5}$
1.600–2.000	1.793	43.63–43.76	43.69	21.8	$(6.48 \pm 0.63) \times 10^{-5}$
1.600–2.000	1.793	43.76–43.88	43.82	22.2	$(4.85 \pm 0.48) \times 10^{-5}$
1.600–2.000	1.793	43.88–44.01	43.94	38.1	$(5.16 \pm 0.37) \times 10^{-5}$
1.600–2.000	1.793	44.01–44.13	44.07	30.5	$(3.30 \pm 0.28) \times 10^{-5}$
1.600–2.000	1.793	44.13–44.26	44.19	38.0	$(3.07 \pm 0.24) \times 10^{-5}$
1.600–2.000	1.793	44.26–44.38	44.32	32.7	$(2.30 \pm 0.20) \times 10^{-5}$
1.600–2.000	1.793	44.38–44.51	44.44	25.3	$(1.35 \pm 0.14) \times 10^{-5}$
1.600–2.000	1.793	44.51–44.63	44.57	18.4	$(9.15 \pm 1.10) \times 10^{-6}$
1.600–2.000	1.793	44.63–44.80	44.72	16.2	$(4.14 \pm 0.54) \times 10^{-6}$
1.600–2.000	1.793	44.80–44.93	44.86	8.3	$(2.14 \pm 0.45) \times 10^{-6}$
1.600–2.000	1.793	44.93–45.05	44.99	3.2	$(8.10 \pm 2.59) \times 10^{-7}$
1.600–2.000	1.793	45.05–45.18	45.11	3.4	$(7.08 \pm 2.55) \times 10^{-7}$
1.600–2.000	1.793	45.18–45.61	45.40	2.1	$(7.76 \pm 2.87) \times 10^{-8}$
1.600–2.000	1.793	45.61–45.86	45.74	0.9	$(1.14 \pm 1.01) \times 10^{-8}$
2.000–2.400	2.194	42.58–43.08	42.83	4.4	$(8.19 \pm 2.29) \times 10^{-5}$
2.000–2.400	2.194	43.08–43.45	43.26	7.1	$(6.74 \pm 1.55) \times 10^{-5}$
2.000–2.400	2.194	43.45–43.63	43.54	6.9	$(5.42 \pm 1.08) \times 10^{-5}$
2.000–2.400	2.194	43.63–43.76	43.69	9.7	$(5.26 \pm 0.74) \times 10^{-5}$
2.000–2.400	2.194	43.76–43.88	43.82	14.8	$(5.46 \pm 0.66) \times 10^{-5}$
2.000–2.400	2.194	43.88–44.01	43.94	23.2	$(5.38 \pm 0.51) \times 10^{-5}$
2.000–2.400	2.194	44.01–44.13	44.07	30.3	$(5.15 \pm 0.43) \times 10^{-5}$
2.000–2.400	2.194	44.13–44.26	44.19	33.3	$(3.63 \pm 0.30) \times 10^{-5}$
2.000–2.400	2.194	44.26–44.38	44.32	25.3	$(2.33 \pm 0.22) \times 10^{-5}$
2.000–2.400	2.194	44.38–44.51	44.44	27.4	$(1.88 \pm 0.18) \times 10^{-5}$
2.000–2.400	2.194	44.51–44.63	44.57	19.9	$(1.19 \pm 0.14) \times 10^{-5}$
2.000–2.400	2.194	44.63–44.80	44.72	17.0	$(5.97 \pm 0.78) \times 10^{-6}$
2.000–2.400	2.194	44.80–44.96	44.88	9.0	$(2.44 \pm 0.44) \times 10^{-6}$
2.000–2.400	2.194	44.96–45.15	45.06	3.7	$(6.00 \pm 1.44) \times 10^{-7}$
2.000–2.400	2.194	45.15–45.39	45.27	2.8	$(2.94 \pm 1.09) \times 10^{-7}$
2.000–2.400	2.194	45.39–45.77	45.58	0.3	$(1.11 \pm 0.51) \times 10^{-8}$
2.000–2.400	2.194	45.77–46.02	45.90	0.9	$(1.22 \pm 1.10) \times 10^{-8}$
2.400–3.000	2.688	42.71–43.21	42.96	3.6	$(5.25 \pm 1.68) \times 10^{-5}$
2.400–3.000	2.688	43.21–43.59	43.40	9.0	$(6.24 \pm 1.12) \times 10^{-5}$
2.400–3.000	2.688	43.59–43.72	43.65	8.5	$(8.04 \pm 1.61) \times 10^{-5}$
2.400–3.000	2.688	43.72–43.84	43.78	7.4	$(4.45 \pm 0.89) \times 10^{-5}$
2.400–3.000	2.688	43.84–43.97	43.90	13.8	$(4.36 \pm 0.57) \times 10^{-5}$
2.400–3.000	2.688	43.97–44.09	44.03	14.0	$(3.09 \pm 0.37) \times 10^{-5}$
2.400–3.000	2.688	44.09–44.22	44.15	22.2	$(3.07 \pm 0.30) \times 10^{-5}$
2.400–3.000	2.688	44.22–44.34	44.28	19.3	$(1.98 \pm 0.22) \times 10^{-5}$
2.400–3.000	2.688	44.34–44.47	44.40	23.9	$(1.61 \pm 0.16) \times 10^{-5}$
2.400–3.000	2.688	44.47–44.59	44.53	21.8	$(1.25 \pm 0.14) \times 10^{-5}$
2.400–3.000	2.688	44.59–44.74	44.67	18.6	$(6.80 \pm 0.75) \times 10^{-6}$

Table 4
(Continued)

z-range	z_c	log L_X-range[a]	log $L_{X,c}$[a]	N_{obj}	$\frac{d\Phi}{d \log L_X}$ [a,b]
2.400–3.000	2.688	44.74–44.87	44.81	12.3	$(4.16 \pm 0.62) \times 10^{-6}$
2.400–3.000	2.688	44.87–45.33	45.10	14.2	$(7.08 \pm 1.06) \times 10^{-7}$
2.400–3.000	2.688	45.33–45.58	45.46	0.6	$(3.99 \pm 1.36) \times 10^{-8}$
3.000–5.800	4.215	42.97–43.47	43.22	2.9	$(7.94 \pm 2.94) \times 10^{-6}$
3.000–5.800	4.215	43.47–43.75	43.61	3.7	$(7.03 \pm 1.76) \times 10^{-6}$
3.000–5.800	4.215	43.75–43.97	43.86	8.5	$(9.67 \pm 1.74) \times 10^{-6}$
3.000–5.800	4.215	43.97–44.10	44.03	5.9	$(5.56 \pm 1.11) \times 10^{-6}$
3.000–5.800	4.215	44.10–44.28	44.19	13.2	$(4.85 \pm 0.68) \times 10^{-6}$
3.000–5.800	4.215	44.28–44.41	44.35	5.5	$(1.70 \pm 0.31) \times 10^{-6}$
3.000–5.800	4.215	44.41–44.53	44.47	8.3	$(1.87 \pm 0.30) \times 10^{-6}$
3.000–5.800	4.215	44.53–44.75	44.64	19.5	$(1.55 \pm 0.19) \times 10^{-6}$
3.000–5.800	4.215	44.75–45.04	44.90	14.4	$(5.38 \pm 0.70) \times 10^{-7}$
3.000–5.800	4.215	45.04–45.29	45.17	4.9	$(1.25 \pm 0.34) \times 10^{-7}$

[a] Units— $\frac{d\Phi}{d \log L_X}$: $[h_{70}^3 \, \mathrm{Mpc}^{-3}\mathrm{dex}^{-1}]$, L_X: $\left[h_{70}^{-2} \mathrm{erg \, s}^{-1} \right]$.

[b] Errors show the 68% confidence range for one parameter ($\Delta \mathcal{L} < 1$).

above in Section 5. The luminosity range of the fit is from log $L_{X,obs} = 41.5$ to 46.0.

The best-fit parameters of Equation (22) for each redshift shell are shown in Table 3. The normalization is defined by

$$A_{44}^{z=z_c} = \frac{d \, \Phi\left(L_X = 10^{44} \, \mathrm{erg \, s}^{-1}, z = z_c\right)}{d \, \log L_X}, \qquad (23)$$

where z_c is the central redshift of the shell, which is defined by $z_c + 1 = \sqrt{\left(1 + z_{min}\right)\left(1 + z_{max}\right)}$, where z_{min} and z_{max} are the minimum and maximum redshifts of the bin. One-sigma parameter errors are calculated in the same way as in Section 5.2. In this section, we have been able to obtain 1σ errors of most parameters with Equation (4), and unlike the case of Section 5.2, the errors of $A_{44}^{z=z_c}$ contain the correlations among the parameter errors. We also show the traditional normalization $A_*^{z=z_c}$ without errors.

Table 4 tabulates the binned N_{obs}/N_{mdl}-estimated XLF for the full treatment case, along with the observed number of AGNs (N_{obs}) and the final estimated XLF value at the center of each bin. The full XLFs in the 11 redshift shells are plotted in Figure 4 in separate panels. The best-fit smoothed two-power-law model (2PL) and the best-fit LDDE model evaluated at z_c are overplotted to assess the goodness of the models. The best-fit two-power-law models at $z_c = 0.1$ (lowest redshift bin) and at $z_c = 1.8$, where the A_{44} is near the peak, are also shown in all panels for reference.

Figure 5 shows the variation of the smoothed two-power-law parameters as a function of redshift. The normalization is the XLF at log $L_X = 44$, and we see the familiar feature of growth (with increasing redshift) between $z = 0$ and $z \sim 1$, followed by a plateau, then a decline at $z > 3$. A notable feature is a sudden drop of the low-luminosity slope γ_1 from $z < 0.6$ ($\gamma_1 \sim 1$), to $z \gtrsim 0.6$ ($\gamma \sim 0.5$). No significant change of slope is observed in each side of this redshift. An F-test comparison between the best-fit models for the case where γ_1 is constant over redshift versus the case where γ_1 changes at $z = 0.6$ shows that the probability that the former is accepted is only 7×10^{-5}. The high-luminosity slope is consistent with being constant at $\gamma_2 \sim 2.7$, except for two data points at $z \sim 0.7$ and $z \sim 1.1$, where γ_2

is significantly smaller, although it may be caused by an observational bias, as discussed in Section 7.

6.3. Evolution of the Space Density in Luminosity Classes

In this section, we investigate the evolution of the AGN space density in different luminosity classes as a function of redshift. We have made the fit to an analytical expression at the center of each of the four luminosity classes: 42.0–43.0, 43.0–44.0, 44.0–45.0, and 45.0–46.0 in log L_X. The XLF at the central luminosity of the bin log L_c, which is defined as the mean of the minimum and maximum bounds of the log L_X bin, can be expressed as

$$\frac{d \, \Phi\left(L_c, z\right)}{d \, \log L_X} = A_{L_c}^{z=0} \cdot e_d\left(z, L_c\right), \qquad (24)$$

where the normalization $A_{L_c}^{z=0}$ is the XLF value at the central luminosity of the class at $z = 0$.

For each luminosity class, we have made a ML fit to the the redshift-dependent evolution parameters in the evolution factor expressed as a three-segment power-law model Equation (18), evaluated at $L_X = L_c$.

During the fitting process, the luminosity dependence of the XLF within the shell is fixed to the best-fit LDDE case. In each class, there are six fitting parameters: $A_{L_c}^{z=0}$, p_1, z_{b1}, p_2, z_{b2}, and p_3. As in the case of redshift-shell-divided samples, ML fits have been made for each luminosity class using Equation (4), where the normalization is also a fitting parameter. Thus the reported normalization errors contain the effects of correlations with other parameters. The resulting best-fit parameters and errors are reported in Table 5.

One limitation of dividing the sample into luminosity classes is that we do not know the intrinsic luminosity L_X of each object. We only know the observed flux and redshift. For the fit of the luminosity class $\left(\log L_{X,min}, \log L_{X,max}\right)$, we select objects that fall into the log $L_{X,min} \leqslant$ log $L_{X,obs} \leqslant$ log $L_{X,max}$ range. Thus the fitting in each luminosity class uses some objects that are outside of the log $L_{X,min} \leqslant$ log $L_{X,obs} \leqslant$ log $L_{X,max}$ range, while others that fall into this range are not used. The fitting process using Equation (9) properly takes care of the expected number of AGNs in the observed
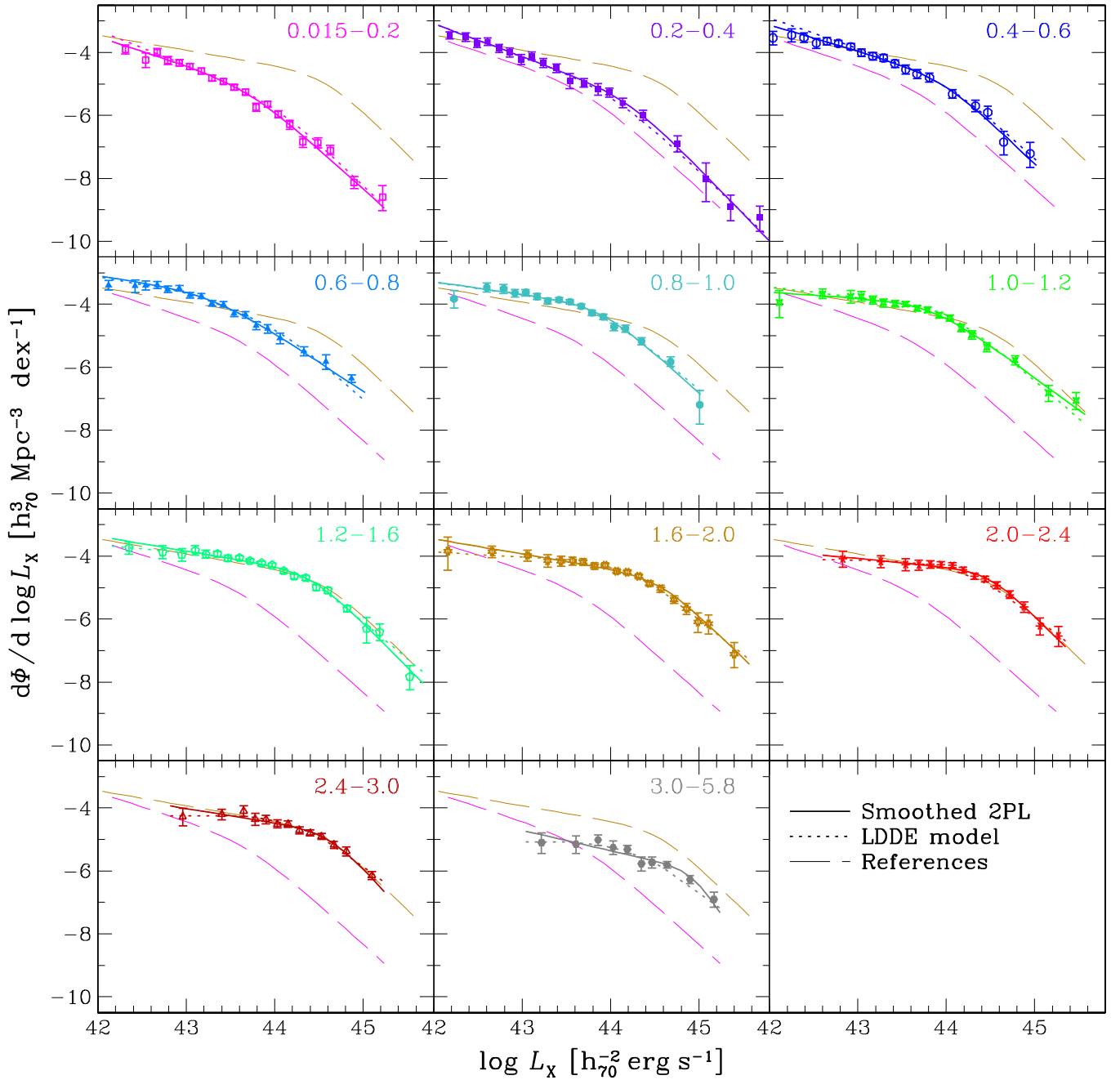
Figure 4. N_{obs}/N_{mdl}-estimated intrinsic 2–10 keV X-ray luminosity function is plotted in each redshift shell as labeled. The 68% approximate Poisson error bars are shown in each data point. The solid line in each panel shows the redshift-divided smoothed 2PL model at the central redshift (z_c). The best-fit LDDE model is shown with dotted lines. The best-fit smoothed two-power-law models for the lowest-redshift shell ($z_c = 0.093$) and at $z_c = 2.214$ are shown with dashed lines in all other panels for reference.

luminosity range calculated based on the intrinsic luminosity XLF model.

Figure 6 shows the evolution of the AGN number density and emissivity in each class for the full treatment. The binned number densities and emissivities, calculated with the N_{obs}/N_{mdl} method using the luminosity-class-divided models, are shown with 68% Poisson errors. The total emissivities of the $42 \leqslant \log L_X [h_{70} \text{ erg s}^{-1}] < 46$ range are also plotted as a function of redshift. The model number densities and emissivities are also shown for the best-fit LDDE model in Table 2 as well as class-divided fits. The evolution of total emissivity in $42 < \log L_X < 46$ is also plotted. Table 6

tabulates the binned N_{obs}/N_{mdl}-estimated values evaluated at the central luminosities L_c (instead of the number densities integrated over the luminosity class, which are plotted in Figure 6), as well as emissivities with best-fit models.

The results in Table 5 show that the first-break redshift z_{b1} increases with luminosity with $z_{b1} \sim 1.1$ at $\log L_X \approx 44$ [h_{70} erg s^{-1}]. The second-break redshift does not vary significantly and is consistent with $z_{b2} \sim 2.7$ at $\log L_X > 43$ [h_{70} erg s^{-1}]. The slope after the second break is consistent with $p_3 \approx -5.6$. These have been fed back as fixed parameters for a refinement of the global expression in Section 5. For the $42 \leqslant \log L_X < 43$ class, the values of z_{b2}
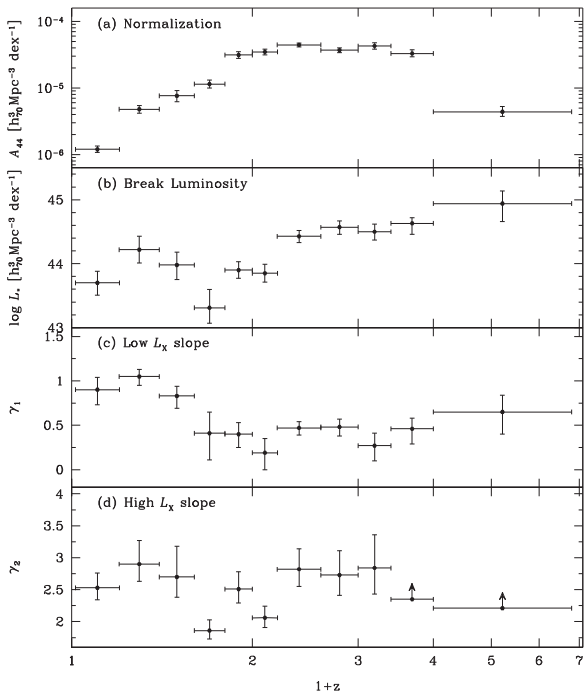
Figure 5. The parameters of the smoothed two-power-law fits to individual redshift shells are plotted as a function of redshift. See labels. The error bars are 1σ, corresponding to $\Delta L = 1$. The upward arrow of in panel (d) corresponds to a 90% lower limit of γ_2.

and p_3 could not be determined because the sample does not extend to the second-break $z_{b2} \sim 2.7$. For the $45 \leqslant \log L_X < 46$ class, the low number of objects has limited our analysis. While we obtain best-fit values of $z_{b1} \approx 1.5$ and $z_{b2} \approx 3$, their 1σ errors are essentially unconstrained. Thus we fixed the $z_{b1} = 1.2$ and $z_{b2} = 2.6$ based on the results of the fit to the $44 \leqslant \log L_X < 45$ class. We have also attempted a two-segment power-law fit (one-break redshift) for this class, but the three-segment form with the two-break redshifts fixed at these values gives a better fit.

While the value of the parameter p_1 increases with luminosity, the measurements are over different redshift ranges for different luminosity classes and should not be compared with one another. The p_2 parameters are also measured over somewhat different redshift ranges. However, it is clear from Figure 6 that the slope between z_{b1} and z_{b2} goes from negative to positive (as a function of log $(1 + z)$) with luminosity. The full binned XLF divided in luminosity classes is shown in Table 6.

Figure 6(a) clearly shows a shift of the number density peak with luminosity up to $\log L_X \approx 44.5$ in the sense that more luminous AGNs (QSOs) peak earlier in the history of the universe, while the low-luminosity ones arise later. Additionally, there is a clear decline of the derived space densities at all luminosity classes. A notable feature is a clear plateau structure at intermediate redshifts at intermediate luminosities, which we have been able to trace in detail thanks to the addition of the COSMOS data set. This has been reflected in the total emissivity curve, which stays almost constant between $1 < z < 2.7$. The slope between the first-break z_{b1} and the second-break z_{b2} changes from negative to positive.

7. DISCUSSION

7.1. Sensitivity to pz-PDZs and Spectral Models

For comparison, we show the parameters for the case where we only take the best-fit single photometric redshift (PZ) per object, instead of full pz-PDFs, under "No PDZ" for the global expression (Table 2). The fitted parameters are not significantly different between the two cases except $p2_{44}$, which is the slope between the first-break and the second-break redshifts at $\log L_X = 44$. The differences in the normalizations are more than the errors given, but these errors are underestimates because for the global expression we use Equation (5), and correlations with other parameters have not been taken into account, as explained in Sections 4.1 and 5.2. To observe the effects more closely, we plot the ratio of the XLF estimates based on the full-PDF and no-PDF samples for each redshift shell in Figure 7. The same are plotted for the number density evolution in each luminosity class in Figure 8. Upon examining the difference between the best-fit models in these figures, the effects of the pz-PDF seem to be as large as ~30% at some locations (blue dashed lines). However, comparing the data points from the N_{obs}/N_{mdl} (black filled hexagonal versus blue open triangle data points in these figures), we see that there is no significant difference, and the apparent discrepancies of the models are at locations that are not well-constrained by the data. Therefore the apparent deviation is not caused by the pz-PDFs, but by the different convergence of the model parameters at the level of a fraction of statistical errors. This is an optimistic case because the COSMOS survey, where the majority of the photometric redshifts with the pz-PDZ came from, has exceptionally high-quality photometric data, achieving an accuracy of $\Delta z/(1 + z) \approx 0.015$ with $\sim$ 5% outliers (Salvato et al. 2011). At the time of our analysis, full pz-PDFs were not available for the CLANS, CLASXS, CDF-N, and CDF-S data in our disposal, in which the spectroscopic redshift completeness ranges from 60–80%. These fractions are similar to those of the LH and COSMOS data set. For these, we take

Table 5
Best-fit Evolution Parameters for Each Luminosity Class

$\log L_X$-range[a]	$\log L_c$[b]	$A_{Lc}^{z=0}$[a]	p_1[a]	z_{b1}[a]	p_2[a]	z_{b2}[a]	p_3[a]
42.0–43.0	42.5	$(8.3 \pm 1.0) \times 10^{-5}$	3.7 ± 0.3	$0.65^{+0.04}_{-0.03}$	$-3.4^{+0.5}_{-0.6}$	...	...
43.0–44.0	43.5	$(6.0 \pm 0.4) \times 10^{-6}$	4.7 ± 0.2	$0.85^{+0.03}_{-0.02}$	$-1.0^{+0.2}_{-0.2}$	$2.69^{+0.10}_{-0.18}$	$-5.9^{+0.0}_{-1.7}$
44.0–45.0	44.5	$(6.8 \pm 0.9) \times 10^{-8}$	$5.8^{+0.2}_{-0.3}$	$1.41^{+0.09}_{-0.11}$	$0.4^{+0.3}_{-0.5}$	$2.63^{+0.16}_{-0.11}$	$-5.4^{+0.9}_{-1.1}$
45.0–46.0	45.5	$\left(8^{+6}_{-4}\right) \times 10^{-11}$	7.3 ± 0.8	1.40^*	2.2 ± 0.9	2.6^*	$-4.7^{+1.2}_{-1.3}$

[a] The same units and error definitions as in Table 3 apply.
[b] Fixed parameters are indicated by an asterisk ("*").
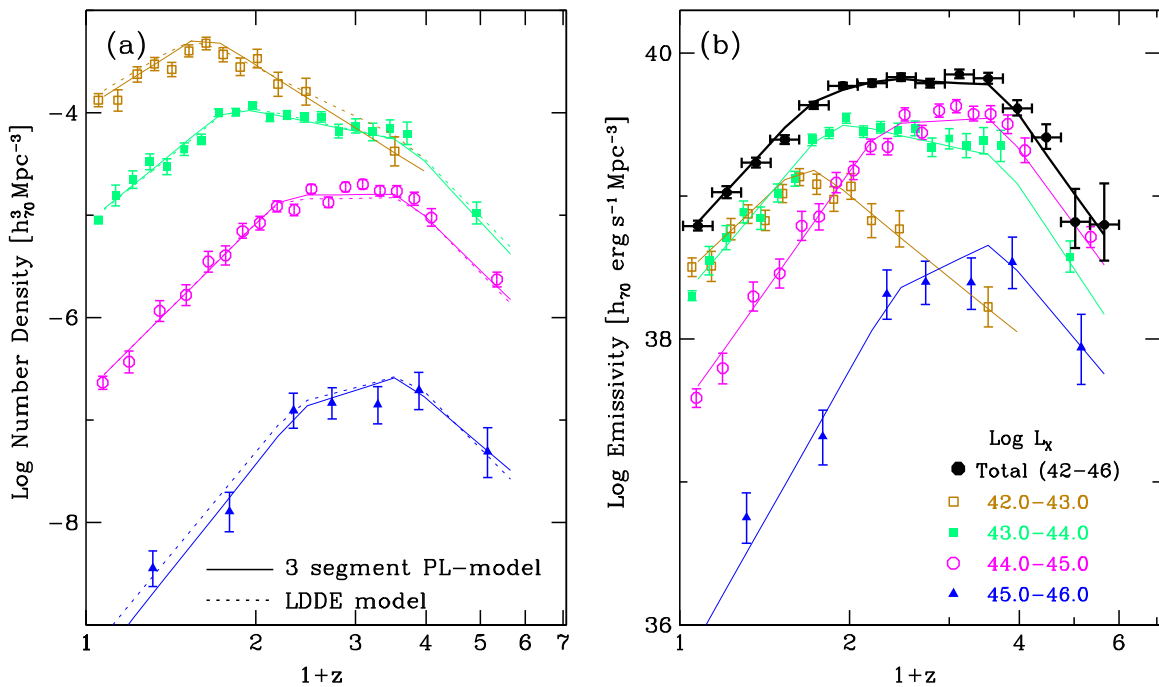
Figure 6. (a) Space density of AGNs as a function of redshift in different luminosity classes as labeled in panel (b). Densities from the luminosity-class-divided fits, as well as those from the LDDE models, are overplotted with solid lines and dotted lines, respectively. (b) The 2–10 keV X-ray emissivities are plotted instead of the number densities. Additionally, the total emissivity curves are added. Only models from the luminosity-divided fits are plotted in this panel.

best-fit photometric redshift values, or for CDF-S sources, if the information about the second peak is available (Luo et al. 2010; Xue et al. 2011), we give a weight of 0.5 in each peak for the full analysis. The photometric redshifts of the CDF-S have a normalized median absolute deviation (NAMD) of $\sigma_{\rm NMAD} = 0.059$ with outliers of 8.6% (Luo et al. 2010), indicating a similar quality to those of COSMOS. Those of the CLANS, CLASXS, and CDF-N surveys use fewer photometric bands, and the uncertainties are as large as $\sigma_z/(1 + z) \sim 0.16$, but with ~6% outliers (Trouille et al. 2008). The uncertainties of these PZ have not been taken into account in our full analysis. For a further test, we create fake PDZ's for objects with photometric redshifts (except those with a second peak) in these surveys with six delta functions. We assume a Gaussian profile centered at the cataloged PZ value $z_{\rm p}$ for the main pz-PDF peak with an appropriate width corresponding to the $\sigma_{\rm NMAD}$ or σ values for each survey. In our fake PDZ, the main peak is represented by three delta functions, one at the center (representing the central half of the PDF main peak), and the others at the 12.5% and 87.5% percentiles of the profile (representing the upper and lower quarter of the PDF main peak). The central one has a weight that is half of 0.5 (1—outlier fraction), and the other two each have a weight that is half of the central one. Also added are three delta functions to represent outliers. Each of the three has a weight of one third of the outlier fraction, and the redshift is taken randomly from spectroscopic redshifts of X-ray sources that have fluxes within a factor of three of that of the object. We keep using the real PDZs for the COSMOS and LH samples. We make global fit the sample, and all the fitted parameters are within a fraction of 1σ error from the original full analysis. Thus we conclude that the uncertainties of the PZs have minimal net effect to our XLF analysis.

In the literature, it has been often assumed for the "hard" $(2 \leqslant E\,[{\rm keV}] \leqslant 7 - 10)$ surveys that absorption is

negligible, and the HXLF is calculated without taking absorption into account, simply by assuming a power-law spectra (e.g., Silverman et al. 2008; Yencho et al. 2009; Aird et al. 2010). For comparison, we also compute the case where all the AGNs have a simple $\Gamma = 1.8$ power law. The results of this case, when PDFs of the photometric redshifts are taken into account, are listed under "$\Gamma = 1.8$" in Table 2 and the comparisons with the "Full" case are overplotted in Figures 7 and 8. As seen in these figures, the XLFs based on the simple spectral assumption of $\Gamma = 1.8$ without the absorption correction are subject to underestimates of the XLF at low luminosities ($\log L_{\rm X} \lesssim 44$) at low redshifts ($z \lesssim 1$), by up to 50%. If one uses a sample selected at $E \gtrsim 5$ keV, however, this systematic error is expected to be reduced dramatically (Fotopoulou et al. 2015).

In principle, the results depend on the $N_{\rm H}$ function and its evolution. Using the 14–195 keV selected *Swift* BAT AGNs with detailed X-ray spectroscopy at $E < 10$ keV and detailed modeling of selection effects, the $N_{\rm H}$ function derived by U14 is robust, especially at low redshifts, and in agreement with that of Burlon et al. (2011) derived using a larger sample of *Swift* BAT AGNs. The fraction of absorbed AGNs among CTN AGNs is observed to increase with redshift (e.g., Hasinger 2008). However, it is not clear whether the increase of absorbed fraction saturates at $z \sim 2$ or keeps increasing to higher redshifts, and Hasinger (2008) commented that a model where the absorption fraction keeps increasing at $z > 2$ is also marginally acceptable. In our analysis above, we have used the U14 result, where the fraction of $22 < \log N_{\rm H} < 24$ AGNs among CTN AGNs at $\log L_{\rm X} = 43.75$ grows as $\propto (1 + z)^{0.45}$ at $(z < 2.0)$ and stays constant at higher redshift. For a sensitivity check, we assume that the absorbed fraction grows as $\propto (1 + z)^{0.32}$ up to our sample limit, where the index has been chosen to have the same absorbed fraction at $z = 3$. The results of the global fit under this assumption have not changed

Table 6
Full Binned XLF Divided in Luminosity Classes

z-range	z_c	$\log L_X$-range[a]	$\log L_{X,c}$[a]	N_{obj}	$\frac{d\Phi}{d L_X}$[a,b]
0.015–0.089	0.051	42.00–43.00	42.50	51.6	$(1.01 \pm 0.13) \times 10^{-4}$
0.089–0.190	0.138	42.00–43.00	42.50	21.2	$(1.02 \pm 0.13) \times 10^{-4}$
0.190–0.276	0.232	42.00–43.00	42.50	38.6	$(1.86 \pm 0.18) \times 10^{-4}$
0.276–0.369	0.322	42.00–43.00	42.50	51.4	$(2.38 \pm 0.20) \times 10^{-4}$
0.369–0.468	0.418	42.00–43.00	42.50	42.9	$(2.13 \pm 0.19) \times 10^{-4}$
0.468–0.575	0.521	42.00–43.00	42.50	57.3	$(3.29 \pm 0.25) \times 10^{-4}$
0.575–0.689	0.631	42.00–43.00	42.50	61.3	$(4.67 \pm 0.34) \times 10^{-4}$
0.689–0.811	0.749	42.00–43.00	42.50	45.6	$(3.60 \pm 0.29) \times 10^{-4}$
0.811–0.942	0.875	42.00–43.00	42.50	29.2	$(2.70 \pm 0.26) \times 10^{-4}$
0.942–1.083	1.011	42.00–43.00	42.50	27.5	$(3.30 \pm 0.33) \times 10^{-4}$
1.083–1.299	1.188	42.00–43.00	42.50	16.9	$(1.86 \pm 0.26) \times 10^{-4}$
1.299–1.615	1.452	42.00–43.00	42.50	14.7	$(1.59 \pm 0.24) \times 10^{-4}$
1.615–3.744	2.522	42.00–43.00	42.50	12.0	$(4.18 \pm 0.67) \times 10^{-5}$
0.015–0.089	0.051	43.00–44.00	43.50	165.3	$(6.56 \pm 0.51) \times 10^{-6}$
0.089–0.168	0.128	43.00–44.00	43.50	22.7	$(1.16 \pm 0.15) \times 10^{-5}$
0.168–0.252	0.209	43.00–44.00	43.50	30.3	$(1.69 \pm 0.19) \times 10^{-5}$
0.252–0.343	0.297	43.00–44.00	43.50	39.5	$(2.55 \pm 0.24) \times 10^{-5}$
0.343–0.440	0.391	43.00–44.00	43.50	34.0	$(2.33 \pm 0.22) \times 10^{-5}$
0.440–0.545	0.492	43.00–44.00	43.50	56.4	$(3.50 \pm 0.26) \times 10^{-5}$
0.545–0.657	0.600	43.00–44.00	43.50	75.7	$(4.42 \pm 0.28) \times 10^{-5}$
0.657–0.777	0.716	43.00–44.00	43.50	140.4	$(8.33 \pm 0.37) \times 10^{-5}$
0.777–0.906	0.840	43.00–44.00	43.50	147.0	$(1.03 \pm 0.05) \times 10^{-4}$
0.906–1.044	0.974	43.00–44.00	43.50	171.3	$(1.16 \pm 0.05) \times 10^{-4}$
1.044–1.192	1.117	43.00–44.00	43.50	126.2	$(9.00 \pm 0.40) \times 10^{-5}$
1.192–1.351	1.270	43.00–44.00	43.50	119.2	$(9.54 \pm 0.44) \times 10^{-5}$
1.351–1.522	1.435	43.00–44.00	43.50	99.1	$(9.13 \pm 0.43) \times 10^{-5}$
1.522–1.704	1.611	43.00–44.00	43.50	83.4	$(9.25 \pm 0.50) \times 10^{-5}$
1.704–1.901	1.801	43.00–44.00	43.50	49.9	$(6.77 \pm 0.43) \times 10^{-5}$
1.901–2.111	2.004	43.00–44.00	43.50	44.7	$(7.66 \pm 0.55) \times 10^{-5}$
2.111–2.336	2.222	43.00–44.00	43.50	32.2	$(6.79 \pm 0.59) \times 10^{-5}$
2.336–2.578	2.455	43.00–44.00	43.50	27.7	$(7.25 \pm 0.70) \times 10^{-5}$
2.578–2.838	2.706	43.00–44.00	43.50	19.5	$(6.56 \pm 0.79) \times 10^{-5}$
2.838–5.309	3.921	43.00–44.00	43.50	20.1	$(1.10 \pm 0.13) \times 10^{-5}$
0.033–0.108	0.070	44.00–45.00	44.50	52.1	$(8.71 \pm 1.22) \times 10^{-8}$
0.108–0.282	0.192	44.00–45.00	44.50	20.3	$(1.45 \pm 0.29) \times 10^{-7}$
0.282–0.422	0.350	44.00–45.00	44.50	21.9	$(4.74 \pm 0.76) \times 10^{-7}$
0.422–0.590	0.504	44.00–45.00	44.50	22.2	$(7.05 \pm 1.06) \times 10^{-7}$
0.590–0.705	0.646	44.00–45.00	44.50	22.4	$(1.55 \pm 0.23) \times 10^{-6}$
0.705–0.829	0.766	44.00–45.00	44.50	25.1	$(1.82 \pm 0.24) \times 10^{-6}$
0.829–0.962	0.894	44.00–45.00	44.50	43.4	$(3.20 \pm 0.29) \times 10^{-6}$
0.962–1.104	1.032	44.00–45.00	44.50	50.5	$(3.96 \pm 0.32) \times 10^{-6}$
1.104–1.256	1.179	44.00–45.00	44.50	71.3	$(5.95 \pm 0.40) \times 10^{-6}$
1.256–1.420	1.337	44.00–45.00	44.50	67.9	$(7.03 \pm 0.46) \times 10^{-6}$
1.420–1.595	1.506	44.00–45.00	44.50	107.7	$(1.33 \pm 0.07) \times 10^{-5}$
1.595–1.784	1.688	44.00–45.00	44.50	76.6	$(1.00 \pm 0.06) \times 10^{-5}$
1.784–1.985	1.883	44.00–45.00	44.50	101.5	$(1.45 \pm 0.07) \times 10^{-5}$
1.985–2.202	2.092	44.00–45.00	44.50	99.7	$(1.57 \pm 0.08) \times 10^{-5}$
2.202–2.434	2.316	44.00–45.00	44.50	78.2	$(1.40 \pm 0.08) \times 10^{-5}$
2.434–2.683	2.556	44.00–45.00	44.50	68.3	$(1.41 \pm 0.08) \times 10^{-5}$
2.683–2.950	2.814	44.00–45.00	44.50	51.7	$(1.20 \pm 0.08) \times 10^{-5}$
2.950–3.236	3.091	44.00–45.00	44.50	29.2	$(7.85 \pm 0.73) \times 10^{-6}$
3.236–5.749	4.347	44.00–45.00	44.50	40.1	$(1.96 \pm 0.16) \times 10^{-6}$
5.749–7.666	6.648	44.00–45.00	44.50	0.0	$<1.1 \times 10^{-6}$
0.173–0.470	0.313	45.00–46.00	45.50	8.1	$(1.03 \pm 0.36) \times 10^{-9}$
0.470–1.190	0.794	45.00–46.00	45.50	6.9	$(4.18 \pm 1.21) \times 10^{-9}$
1.190–1.480	1.330	45.00–46.00	45.50	8.6	$(4.45 \pm 1.20) \times 10^{-8}$
1.480–2.000	1.728	45.00–46.00	45.50	10.5	$(5.67 \pm 1.13) \times 10^{-8}$
2.000–2.600	2.286	45.00–46.00	45.50	7.9	$(5.93 \pm 1.19) \times 10^{-8}$
2.600–3.200	2.888	45.00–46.00	45.50	7.7	$(8.42 \pm 1.77) \times 10^{-8}$
3.200–5.310	4.148	45.00–46.00	45.50	4.6	$(2.13 \pm 0.55) \times 10^{-8}$

[a] Units—$\frac{d\Phi}{d \log L_X}$: $[h_{70}^3 \; \mathrm{Mpc}^{-3}\mathrm{dex}^{-1}]$, L_X: $\left[h_{70}^{-2}\mathrm{erg \; s}^{-1} \right]$.

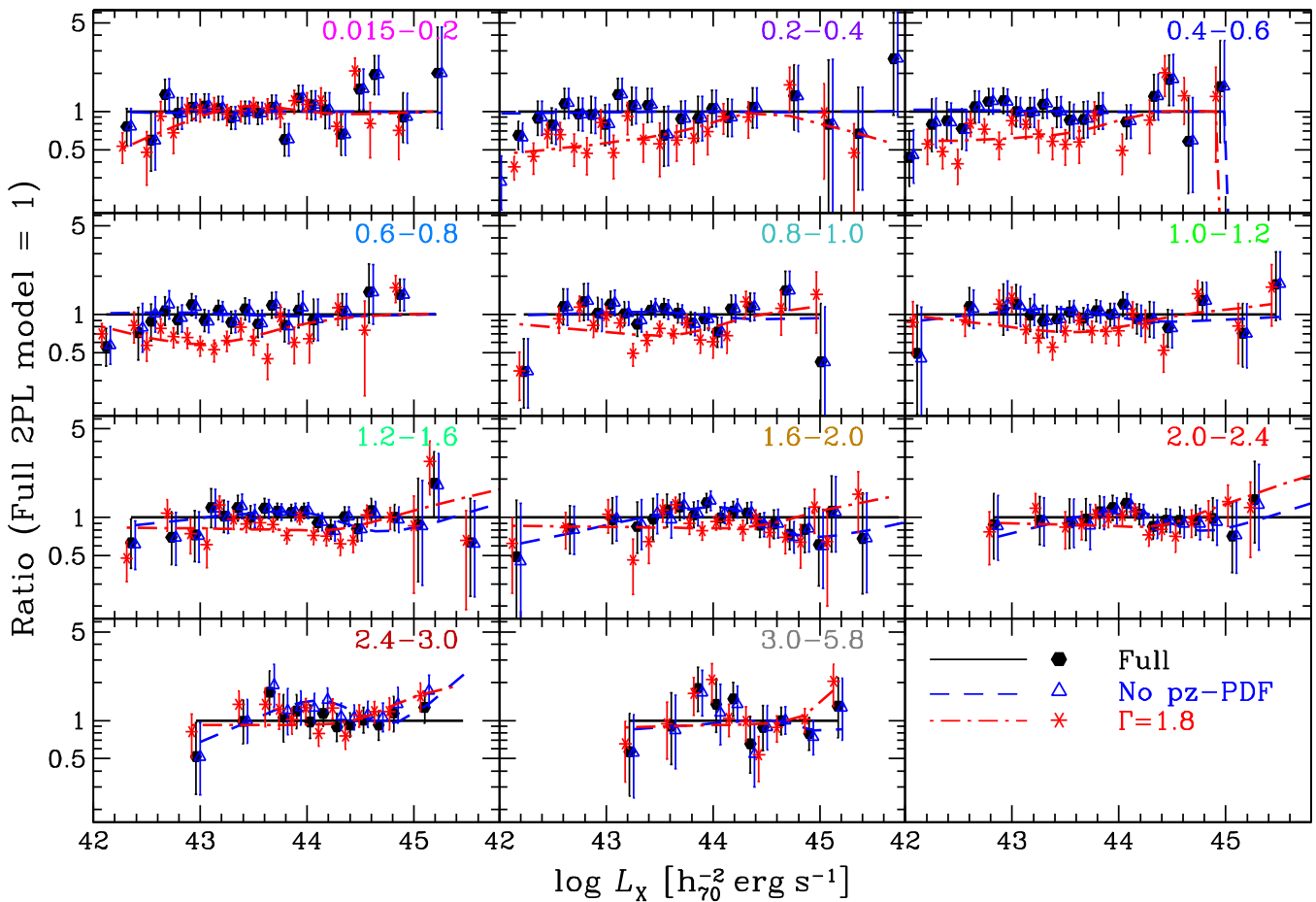[b] Errors show the 68% confidence range for one parameter ($\Delta\mathcal{L} < 1$). The symbol "<" shows a 90% upper limit.

Figure 7. Comparison of best-fit models in each redshift shell and the N_{obs}/N_{mdl} estimates. The best-fit two-power-law models of the case of the no pz-PDFs and $\Gamma = 1.8$ are divided by those of the full case. The N_{obs}/N_{mdl} XLFs are also divided by the full model. See labels in the lowest rightmost panel for the meanings of line styles, symbols, and colors (electronic version). The data points of the no-PDF and $\Gamma = 1.8$ cases are shifted horizontally by $+0.04$ and -0.04, respectively, in log L_X for display purposes.

significantly, and all the parameters are consistent with our "Full" case within a fraction of 1σ. This can be understood because, at high redshift, the 0.5–10 keV band, which is usually used for the spectral analysis or hardness ratio analysis to measure N_H, corresponds to rest-frame $E > 1.5$ keV at $z > 2$. Thus it is already not sensitive to measuring absorption. For the same reason, from the 2–10 keV flux, we measure rest-frame higher-energy luminosity, which has not been affected by absorption. Since we want to derive the intrinsic XLF, the measured X-ray luminosity is insensitive to the details of the N_H function at high redshifts.

7.2. Detailed Behavior of the XLF

Thanks to the addition of the COSMOS data set, we have been able to trace the detailed behavior of the XLF in the intermediate-redshift/intermediate-luminosity range. We describe a number of notable features.

1. The low-luminosity slope γ_1 flattens suddenly at $z \sim$ 0.6. The slopes stay almost constant within each of the $z < 0.6$ and $z \gtrsim 0.6$ regimes, having $\gamma_1 \approx 1$ and ≈ 0.5 respectively. This sudden flattening of the slope practically excludes ILDE/LADE models, where the shape of the XLF stays unchanged over redshift, as a global expression. The high-redshift faint-end slope is consistent with those of optically selected QSOs at

$1 \lesssim z \lesssim 3.5$ ($\gamma_1 \sim 0.45$) measured by Bongiorno et al. (2007) and $z \sim 4$ QSOs by Ikeda et al. (2011) ($\gamma_1 = 0.7 \pm 0.2$). Note, however, that the faint-end slope measured by Glikman et al. (2010) is significantly steeper ($\gamma_1 = 1.3 \pm 0.2$ at $z \sim 4$).

2. The high-luminosity slope stays almost constant ($\gamma_2 \approx 2.7$), with the exception of two redshift shells at $0.6 < z < 0.8$ and $1.0 < z < 1.2$, which have flatter slopes $\gamma_2 \approx 2.0$. For the shell between these ($0.8 < z < 1.0$), γ_2 is consistent with those for the rest of the shells. We note that the high-luminosity end of the XLF is poorly sampled at these redshifts, and the apparently low γ_2 values may be caused by the higher weights at luminosities just above the break and less weight at the highest luminosities. Thus there is no evidence for systematic change of the high-luminosity slope with redshift. The upcoming *eROSITA* mission will provide better sampling of this regime, which will enable us to see if the high end slope is constant over all redshifts.

3. The addition of the new data including COSMOS revealed new details about AGN downsizing. The number density/emissivity growth curves have two distinctive breaks, one at $z_{b1} \approx 1$ and the other at $z_{b2} \approx$ 2.7, with a "plateau" between them. In any luminosity class, a rapid rise of number density with cosmic time is observed above z_{b2} (except the lowest-luminosity bin),
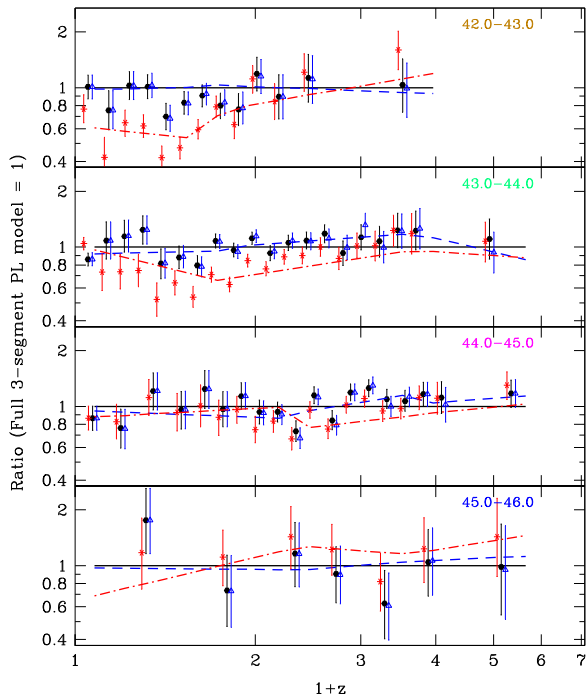
Figure 8. Comparison of best-fit models and the N_{obs}/N_{mdl} estimates in each luminosity class. The best-fit three-segment power-law models of the no-pz-PDF and $\Gamma = 1.8$ cases are divided by those of the full case. The N_{obs}/N_{mdl} XLFs are also divided by the full model. The data points of the no-pz-PDF and $\Gamma = 1.8$ cases are shifted horizontally by $+0.007$ and -0.007, respectively, in $\log (1 + z)$ for display purposes. See Figure 7 for the meanings of line styles, symbols, and colors.

and a rapid decline is observed after z_{b1}. At low luminosities, ($\log L_X \lesssim 44$), the peak is at z_{b1}, and at high luminosities, ($\log L_X \lesssim 44$), z_{b2} becomes the peak. Additionally, the position of the first break moves from lower to higher redshifts with luminosity up from $z \sim 0.6$ to $z \sim 1.4$ up to $\log L_X \lesssim 44.5$. No evidence for a change in z_{b2} with luminosity is observed.

Our results are in excellent agreement with those of U14, as seen in Figure 9(a). Small excesses at the level of $\lesssim 0.2$ dex at a few data points can be well explained by cosmic variance. Especially our a few $\times 10^{-15} \lesssim S_{X,obs} \lesssim 10^{-14}$ erg s^{-1} cm^{-2} range is dominated by the COSMOS data, which may be affected by large-scale structures seen as redshift spikes (Gilli et al. 2009; Brusa et al. 2010; Civano et al. 2012). Other possible differences at the same level may be explained in the treatment of the probability density distribution of the photometric redshifts. Our results at the highest-redshift shell $z > 3$, as well as the redshift evolution factor (p_3), are consistent with the recent results by Vito et al. (2014).

7.3. Comparison with Theoretical Models

There are a number of attempts to reproduce/understand the downsizing behavior of AGN evolution within cosmological simulations and semianalytical models (SAMs). In order to understand the implication of our results to the physical scenarios on accretion processes by comparing observations and theory, we should consider which features of the theoretical predictions are a consequence of the assumed physical picture and which features are a consequence of

adjusting free parameters to match the AGN luminosity functions in various redshifts.

In their attempt to reproduce the faint-end AGN LF, Degraf et al. (2010) considered a BH growth by infall of surrounding gas via Bondi (1952) accretion, which some authors call "radio mode" or "hot halo mode," and merging with other BHs in their simulations, including the hydrodynamic gas component. They compared their results with luminosity-class-divided number density evolution curves of soft (Hasinger et al. 2005) and hard X-ray (Ueda et al. 2003) selected AGNs. They recognize that their model overproduces number densities of X-ray-selected AGNs at $z > 1$. We compare our number density evolution with two SAMs of Marulli et al. (2008) and Fanidakis et al. (2012), where we have been able to convert their published results to the density curves in our 2–10 keV luminosity classes in Figure 9(a). This figure shows that the overproduction is also seen in these SAMs.

Since these authors did not provide the number density curves in the 2–10 keV range, we explain the derivation of the luminosity-class-divided 2–10 keV number density curves from their published figures. For Marulli et al. (2008), we use their Figure 7 and take the "best" bolometric luminosity function model. The bolometric LF has been converted to the 2–10 keV XLF model using the bolometric correction by Hopkins et al. (2007) and integrated over our luminosity classes. For Fanidakis et al. (2012), we use their soft (0.5–2 keV) X-ray "before obscuration (total)" curves provided in their Figure 18 (b) instead of their "after obscuration (visible)" curves to compare with our 2–10 keV density evolution curves. We convert their "before obscuration" curves to those for 2–10 keV assuming a photon index of $\Gamma = 1.9$, which is representative of unobscured AGNs. Since they use slightly different cosmological parameters, we also convert the density curves to our adopted cosmology to overplot in Figure 9(a).

In both cases, we see overpredictions of AGN number density at highest redshift at low-luminosity bins. As AGN model components, the Marulli et al. (2008) model took into account the "radio"-mode accretion and merger-driven "quasar" mode. The Fanidakis et al. (2012) model took into account the "radio" and the "starburst" modes, where the "starburst mode" includes merger-driven "quasar mode" and secular (disk instability) components. Marulli et al. (2008) considered a number of AGN light curve models and searched for the one that fits well with the bolometric LF of Hopkins et al. (2007) and thus had freedom in adjusting to the observations. On the other hand, Fanidakis et al. (2012) had four free parameters to fit to the LF. Except for the duty cycle, which is adjusted to the global normalization of the LF, the parameters are physically motivated. The Fanidakis et al. (2012) model overpredicts the number densities at high redshift at all luminosity classes. In their comparison with the 0.5–2 keV XLF, they took into account the effects of luminosity dependence and redshift evolution of obscured/type-2 AGN fraction f_2 by Hasinger (2008). For the redshift evolution of f_2, Hasinger (2008) proposed a model with $f_2 \propto (1 + z)^{0.62}$ up to $z = 2.06$ and which stays constant at higher redshifts as preferred, while Fanidakis et al. (2012) used a marginally acceptable model with $f_2 \propto (1 + z)^{0.48}$ without saturation, and thus their obscured fraction keeps increasing to higher redshifts. The latter form of the obscured fraction evolution was needed in the model of Fanidakis et al. (2012) for satisfactory consistencies with the optical QSO and
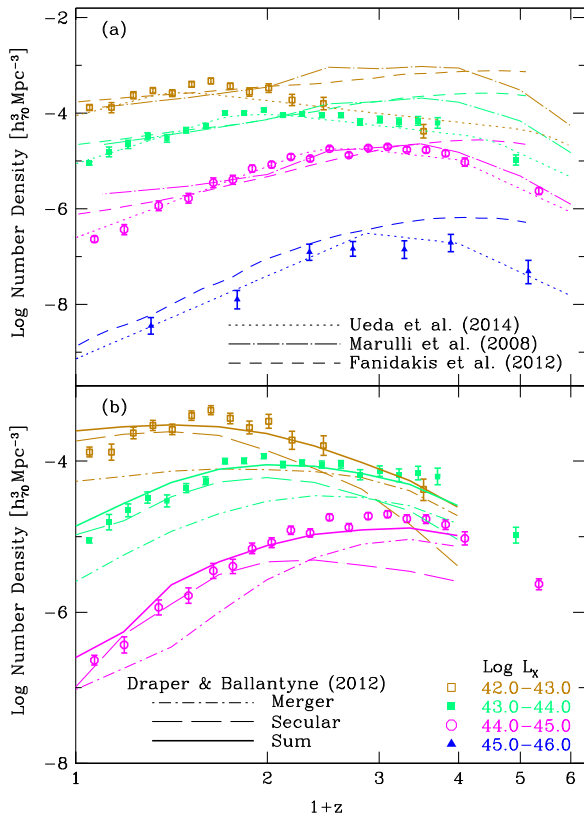
Figure 9. (a) Our luminosity-class-divided number density evolution curves (binned data points with error bars from Figure 6(a)) are compared with the LDDE model from recent comparable work by Ueda et al. (2014; dotted lines). Additionally, results from recent semianalytical models from the literature from Marulli et al. (2008; dotted–dashed lines) and Fanidakis et al. (2012; dashed lines) are overplotted. Luminosity classes for the data points and model curves are indicated by colors as labeled. See text for detailed conversions of their published results to the 2–10 keV density curves. Model by Marulli et al. (2008) does not reach the highest-luminosity bin, and therefore we are not able to plot the log $L_X = 45–46$ bin. (b) The same number density curves are compared with the model by Draper & Ballantyne (2012; solid lines) with separate contributions from merger (dotted lines) and secular processes (dashed lines).

soft XLF to their model. On the other hand, the high-z overprediction of the 2–10 keV number densities shows that they indeed overpredicted the high-redshift AGN population and overcorrected for the effects of obscuration to match with the 0.5–2 keV number density/optical QSOs. The tendency of overprediction of the high-redshift, low-luminosity/mass population is also a problem with predicting the stellar mass function of galaxies (e.g., Guo et al. 2011), the reason for which is still unclear. On the other hand, if their basic prediction on high-redshift accretion is correct, the discrepancy may be an indication of a large population of highly CTK AGNs at high redshifts. The high-redshift overprediction problem is also present in the recent model by Sijacki et al. (2014) at all luminosities.

Another interesting model is by Draper & Ballantyne (2012), in which they considered merger and secular modes of AGNs triggering. Their work was not directly based on cosmological simulations. Instead they took simple formulae for the evolution of galaxy number density with stellar mass above some threshold value, gas fraction, and merger rate from the literature. They then considered secular and merger-driven AGN triggering followed by a parameterized model of

luminosity decay. Their model 2–10 keV number density evolutions are overplotted with our data in Figure 9(b), which has been derived from their Figure 7. Since their Figure 7 shows curves for log $L_X > 42$, >43, and >44, we draw their model curves of the log $L_X = 42–43$ and 43–44 curves by subtracting their >43 curve from the >42 one, and their >44 curve from the >43 one, respectively. For the 44–45 curve, we use their >44 curve, since the contribution of the log $L_X > 45$ AGNs to the number density is only ∼ 0.2% of the >44 AGNs for $\gamma_2 = 2.7$. We see that their "sum" of the contributions of the two processes is in good agreement with our data. Since they have three free parameters to adjust in their AGN light curves, which are the timescale, slope of the decay, and the peak Eddington ratio, they had much freedom in adjusting to the observed XLFs. Thus it is no surprise that their theoretical curves agree well with our observation. However, they had difficulties in reproducing the hard X-ray number density curve with only one mode, i.e., merger only or secular only. Their summed curves show the flat-top (two-break) structures, where the slope in the $z_{b1} < z < z_{b2}$ range increases from negative to positive with luminosity.

8. CONCLUSIONS

We have investigated the detailed behavior of the intrinsic 2–10 keV XLF of AGNs from a combination of samples in various depths/width. We summarize our conclusions.

1. A total of ∼3200 unique X-ray AGNs from a combination of wide to deep samples covering the redshifts of $0.015 < z < 5.8$, and six orders of magnitude in flux have been used to investigate the behavior of the XLF. In particular, we present here the XLF from X-ray sources from both of the *XMM* and *Chandra* COSMOS surveys, which comprise about 43% of our global sample.

2. Recent N_H functions and realistic spectral templates are fully incorporated in the ML fitting to analytic expressions, as well as the N_{obs}/N_{mdl}-estimated binned intrinsic XLF. The photometric redshift probability density distributions (pz-PDFs) of the COSMOS and Lockman Hole samples, as well as secondary photometric redshifts of CDF-S, are also considered.

3. We present a full parametric LDDE model and redshift - shell and luminosity-class-separated models, as well as the binned XLF, using the N_{obs}/N_{mdl} estimator.

4. The low luminosity end slope of the XLF flattens suddenly at $z > 0.6$. This behavior practically excludes any global expression of XLF evolution that assumes an unchanged XLF shape over cosmic time.

5. We investigate the net effects of ignoring probability density distribution (pz-PDF) of photometric redshifts. The effect of including pz-PDF into the analysis does not alter the final XLF results significantly.

6. We investigate the effects of assuming a simple AGN spectrum of $\Gamma = 1.8$. Under this simple assumption, the XLF is subject to underestimates by up to ∼50% in the low-redshift, low-luminosity regime.

7. The detailed behaviors of AGN downsizing have been revealed. A clear two-break structure has been revealed in the number density evolution curves at every luminosity class above log $L_X > 43$. This behavior is qualitatively consistent with a two-mode AGN evolution involving major merger and secular processes.

8. Most current SAMs of AGNs overproduce AGN number densities in the high-redshift, low-luminosity regime. Their semianalytical treatment of accretion processes may have to be revised to reproduce our results. Alternatively, if their accretion scenario is correct, this may suggest a population of heavily CTK AGNs in this regime.

Note added in proof. After submission of the final version of this paper, we received a preprint by Aird et al. (2015). While their methods and samples are significantly different, many of their results are the same as those of this work.

REFERENCES

Aird, J., Coil, A. L., Georgakakis, A., et al. 2015, MNRAS, submited (arXiv:1503.01120)
Aird, J., Nandra, K., Laird, E. S., et al. 2010, MNRAS, 401, 2531
Ajello, M., Alexander, D. M., Greiner, J., et al. 2012, ApJ, 749, 21
Akiyama, M., Ohta, K., Yamada, T., et al. 2000, ApJ, 532, 700
Akiyama, M., Ueda, Y., Ohta, K., Takahashi, T., & Yamada, T. 2003, ApJS, 148, 275
Allevato, V., Finoguenov, A., Cappelluti, N., et al. 2011, ApJ, 736, 99
Allevato, V., Finoguenov, A., Hasinger, G., et al. 2012, ApJ, 758, 47
Alexander, D. M., Bauer, F. E., Brandt, W. N., et al. 2003, AJ, 126, 539
Alexander, D. M., Stern, D., Del Moro, A., et al. 2013, ApJ, 773, 125
Avni, Y., & Bahcall, J. N. 1980, ApJ, 235, 694
Baldi, A., Molendi, S., Comastri, A., et al. 2002, ApJ, 564, 190
Barcons, X., Carrera, F. J., Ceballos, M. T., et al. 2007, A&A, 476, 1191
Beckmann, V., Soldi, S., Ricci, C., et al. 2009, A&A, 505, 417
Bondi, H. 1952, MNRAS, 112, 195
Bongiorno, A., Zamorani, G., Gavignaud, I., et al. 2007, A&A, 472, 443
Boyle, B. J., Griffiths, R. E., Shanks, T., Stewart, G. C., & Georgantopoulos, I. 1993, MNRAS, 260, 49
Brandt, W. N., & Hasinger, G. 2005, ARA&A, 43, 827
Brightman, M., & Ueda, Y. 2012, MNRAS, 423, 702
Brightman, M., Nandra, K., Salvato, M., Hsu, L.-T., & Rangel, C. 2014, MNRAS, 443, 1999
Brunner, H., Cappelluti, N., Hasinger, G., et al. 2008, A&A, 479, 283
Brusa, M., Civano, F., Comastri, A., et al. 2010, ApJ, 716, 348
Brusa, M., Zamorani, G., Comastri, A., et al. 2007, ApJS, 172, 353
Buchner, J., Georgakakis, A., Nandra, K., et al. 2015, ApJ, 802, 89
Burlon, D., Ajello, M., Greiner, J., et al. 2011, ApJ, 728, 58
Cappelluti, N., Hasinger, G., Brusa, M., et al. 2007, ApJS, 172, 341
Cappelluti, N., Brusa, M., Hasinger, G., et al. 2009, A&A, 497, 635
Cappelluti, N., Ajello, M., Burlon, D., et al. 2010, ApJL, 716, L209
Civano, F., Elvis, M., Brusa, M., et al. 2012, ApJS, 201, 30
Cocchia, F., Fiore, F., Vignali, C., et al. 2007, A&A, 466, 31
Coil, A. L., Georgakakis, A., Newman, J. A., et al. 2009, ApJ, 701, 1484
Croton, D. J. 2009, MNRAS, 394, 1109
Chatterjee, S., Nguyen, M. L., Myers, A. D., & Zheng, Z. 2013, ApJ, 779, 147
Cowie, L. L., Barger, A. J., Bautz, M. W., et al. 2003, ApJL, 584, L57
Degraf, C., Di Matteo, T., & Springel, V. 2010, MNRAS, 402, 1927

Della Ceca, R., Maccacaro, T., Caccianiga, A., et al. 2004, A&A, 428, 383
Della Ceca, R., Caccianiga, A., Severgnini, P., et al. 2008, A&A, 487, 119
Di Matteo, T., Croft, R. A. C., Springel, V., & Hernquist, L. 2003, ApJ, 593, 56
Draper, A. R., & Ballantyne, D. R. 2012, ApJ, 751, 72
Ebrero, J., Carrera, F. J., Page, M. J., et al. 2009, A&A, 493, 55
Elvis, M., Civano, F., Vignali, C., et al. 2009, ApJS, 184, 158
Fanidakis, N., Baugh, C. M., Benson, A. J., et al. 2012, MNRAS, 419, 2797
Fanidakis, N., Georgakakis, A., Mountrichas, G., et al. 2013, MNRAS, 435, 679
Fiore, F., Brusa, M., Cocchia, F., et al. 2003, A&A, 409, 79
Fotopoulou, S., Buchner, J., Gerogantopoulos, I., et al. 2015, A&A, submitted
Fotopoulou, S., Salvato, M., Hasinger, G., et al. 2012, ApJS, 198, 1
Gehrels, N. 1986, ApJ, 303, 336
Georgakakis, A., Pérez-González, P. G., Fanidakis, N., et al. 2014, MNRAS, 440, 339
Georgantopoulos, I., Akylas, A., Georgakakis, A., & Rowan-Robinson, M. 2009, A&A, 507, 747
Glikman, E., Bogosavljević, M., Djorgovski, S. G., et al. 2010, ApJ, 710, 1498
Gilli, R., Zamorani, G., Miyaji, T., et al. 2009, A&A, 494, 33
Gültekin, K., Richstone, D. O., Gebhardt, K., et al. 2009, ApJ, 698, 198
Guo, Q., White, S., Boylan-Kolchin, M., et al. 2011, MNRAS, 413, 101
Häring, N., & Rix, H.-W. 2004, ApJL, 604, L89
Hasinger, G., Altieri, B., Arnaud, M., et al. 2001, A&A, 365, L45
Hasinger, G., Miyaji, T., & Schmidt, M. 2005, A&A, 441, 417
Hasinger, G., Cappelluti, N., Brunner, H., et al. 2007, ApJS, 172, 29
Hasinger, G. 2008, A&A, 490, 905
Hiroi, K., Ueda, Y., Hayashida, M., et al. 2013, ApJS, 207, 36
Hopkins, P. F., Hernquist, L., Cox, T. J., et al. 2005, ApJ, 630, 716
Hopkins, P. F., Richards, G. T., & Hernquist, L. 2007, ApJ, 654, 731
Ikeda, H., Nagao, T., Matsuoka, K., et al. 2011, ApJL, 728, L25
James, F. 1994, MINUIT Reference Manual, CERN Program Library Long Writeup D506 (Geneva: CERN)
Jones, L. R., McHardy, I. M., Merrifield, M. R., et al. 1997, MNRAS, 285, 547
Kormendy, J., & Ho, L. C. 2013, ARA&A, 51, 511
Krumpe, M., Miyaji, T., & Coil, A. L. 2010, ApJ, 713, 558
Krumpe, M., Miyaji, T., Coil, A. L., & Aceves, H. 2012, ApJ, 746, 1
Lanzuisi, G., Ranalli, P., Georgantopoulos, I., et al. 2015, A&A, 573, AA137
Lehmer, B. D., Xue, Y. Q., Brandt, W. N., et al. 2012, ApJ, 752, 46
Luo, B., Brandt, W. N., Xue, Y. Q., et al. 2010, ApJS, 187, 560
La Franca, F., & Cristiani, S. 1997, AJ, 113, 1517
La Franca, F., Fiore, F., Comastri, A., et al. 2005, ApJ, 635, 864
Magorrian, J., Tremaine, S., Richstone, D., et al. 1998, AJ, 115, 2285
Mignoli, M., Pozzetti, L., Comastri, A., et al. 2004, A&A, 418, 827
Maiolino, R., Mignoli, M., Pozzetti, L., et al. 2006, A&A, 445, 457
Marshall, H. L., Tananbaum, H., Avni, Y., & Zamorani, G. 1983, ApJ, 269, 35
Marulli, F., Bonoli, S., Branchini, E., Moscardini, L., & Springel, V. 2008, MNRAS, 385, 1846
Miyaji, T., Hasinger, G., & Schmidt, M. 2000a, A&A, 353, 25 (paper I)
Miyaji, T., Hasinger, G., & Schmidt, M. 2000b, AdSpR, 25, 827
Miyaji, T., Hasinger, G., & Schmidt, M. 2001, A&A, 369, 49 (paper II)
Miyaji, T., Zamorani, G., Cappelluti, N., et al. 2007, ApJS, 172, 396
Miyaji, T., Krumpe, M., Coil, A. L., & Aceves, H. 2011, ApJ, 726, 83
Mullis, C. R., Henry, J. P., Gioia, I. M., et al. 2004, ApJ, 617, 192
Page, M. J., Mason, K. O., McHardy, I. M., Jones, L. R., & Carrera, F. J. 1997, MNRAS, 291, 324
Page, M. J., & Carrera, F. J. 2000, MNRAS, 311, 433
Persic, M., Rephaeli, Y., Braito, V., et al. 2004, A&A, 419, 849
Ranalli, P., Comastri, A., & Setti, G. 2005, A&A, 440, 23
Ptak, A., Mobasher, B., Hornschemeier, A., Bauer, F., & Norman, C. 2007, ApJ, 667, 826
Polletta, M., Tajer, M., Maraschi, L., et al. 2007, ApJ, 663, 81
Puccetti, S., Vignali, C., Cappelluti, N., et al. 2009, ApJS, 185, 586
Richardson, J., Chatterjee, S., Zheng, Z., Myers, A. D., & Hickox, R. 2013, ApJ, 774, 143
Salvato, M., Hasinger, G., Ilbert, O., et al. 2009, ApJ, 690, 1250
Salvato, M., Ilbert, O., Hasinger, G., et al. 2011, ApJ, 742, 61
Schmidt, M., & Green, R. F. 1983, ApJ, 269, 352
Schneider, P. 2006, Extragalactic Astronomy and Cosmology: An Introduction (Berlin: Springer)
Scoville, N., Aussel, H., Brusa, M., et al. 2007, ApJS, 172, 1
Sijacki, D., Vogelsberger, M., Genel, S., et al. 2014, arXiv:1408.6842
Silverman, J. D., Green, P. J., Barkhouse, W. A., et al. 2008, ApJ, 679, 118
Taniguchi, Y., Scoville, N., Murayama, T., et al. 2007, ApJS, 172, 9
Treister, E., Urry, C. M., & Virani, S. 2009, ApJ, 696, 110
Trouille, L., Barger, A. J., Cowie, L. L., Yang, Y., & Mushotzky, R. F. 2008, ApJS, 179, 1

Trouille, L., Barger, A. J., Cowie, L. L., Yang, Y., & Mushotzky, R. F. 2009, ApJ, 703, 2160

Tueller, J., Baumgartner, W. H., Markwardt, C. B., et al. 2010, ApJS, 186, 378

Ueda, Y., Takahashi, T., Inoue, H., et al. 1998, Natur, 391, 866

Ueda, Y., Takahashi, T., Inoue, H., et al. 1999, ApJ, 518, 656

Ueda, Y., Ishisaki, Y., Takahashi, T., Makishima, K., & Ohashi, T. 2001, ApJS, 133, 1

Ueda, Y., Akiyama, M., Ohta, K., & Miyaji, T. 2003, ApJ, 598, 886

Ueda, Y., Ishisaki, Y., Takahashi, T., Makishima, K., & Ohashi, T. 2005, ApJS, 161, 185

Ueda, Y., Hiroi, K., Isobe, N., et al. 2011, PASJ, 63, 937

Ueda, Y., Akiyama, M., Hasinger, G., Miyaji, T., & Watson, M. G. 2014, ApJ, 786, 104

Vito, F., Gilli, R., Vignali, C., et al. 2014, MNRAS, 445, 3557

Wyithe, J. S. B., & Loeb, A. 2003, ApJ, 595, 614

Xue, Y. Q., Luo, B., Brandt, W. N., et al. 2011, ApJS, 195, 10

Yang, Y., Mushotzky, R. F., Steffen, A. T., Barger, A. J., & Cowie, L. L. 2004, AJ, 128, 1501

Yang, Y., Mushotzky, R. F., Barger, A. J., & Cowie, L. L. 2006, ApJ, 645, 68

Yencho, B., Barger, A. J., Trouille, L., & Winter, L. M. 2009, ApJ, 698, 380